

UCSF

UC San Francisco Previously Published Works

Title

An ultrapotent synthetic nanobody neutralizes SARS-CoV-2 by stabilizing inactive Spike

Permalink

<https://escholarship.org/uc/item/1ks1d323>

Journal

Science, 370(6523)

ISSN

0036-8075

Authors

Schoof, Michael

Faust, Bryan

Saunders, Reuben A

et al.

Publication Date

2020-12-18

DOI

10.1126/science.abe3255

Peer reviewed

1 **An ultra-high affinity synthetic nanobody blocks SARS-CoV-2 infection by locking Spike**  
2 **into an inactive conformation**

3  
4 Michael Schoof<sup>1,2##</sup>, Bryan Faust<sup>1,2,3,4#</sup>, Reuben A. Saunders<sup>1,5#</sup>, Smriti Sangwan<sup>1,2#</sup>, Veronica  
5 Rezelj<sup>6#</sup>, Nick Hoppe<sup>3,4</sup>, Morgane Boone<sup>1,2</sup>, Christian Bache Billesbølle<sup>3,4</sup>, Marcell Zimanyi<sup>1,2,3</sup>,  
6 Ishan Deshpande<sup>3,4</sup>, Jiahao Liang<sup>3</sup>, Aditya A. Anand<sup>1,2</sup>, Niv Dobzinski<sup>1,2</sup>, Beth Shoshana Zha<sup>7</sup>,  
7 Benjamin Barsi-Rhynch<sup>3</sup>, Vladislav Belyy<sup>1,2</sup>, Andrew W. Barile-Hill<sup>8</sup>, Sayan Gupta<sup>9</sup>, Camille R.  
8 Simoneau<sup>10,11,12</sup>, Kristoffer Leon<sup>10,11,12</sup>, Kris M. White<sup>13,14</sup>, Silke Nock<sup>1,2</sup>, Yuwei Liu<sup>1,2</sup>, Nevan J.  
9 Krogan<sup>4,5,10,11</sup>, Corie Y. Ralston<sup>9</sup>, Danielle L. Swaney<sup>4,5,10,11</sup>, Adolfo García-Sastre<sup>13,14</sup>, Melanie  
10 Ott<sup>10,11,12</sup>, Marco Vignuzzi<sup>6</sup>, QCRG Structural Biology Consortium<sup>4</sup>, Peter Walter<sup>1,2\*</sup>, Aashish  
11 Manglik<sup>3,4,10,15\*</sup>

12  
13 <sup>1</sup>Howard Hughes Medical Institute, University of California at San Francisco, San Francisco, CA,  
14 USA.

15 <sup>2</sup>Department of Biochemistry and Biophysics, University of California at San Francisco, San  
16 Francisco, CA, USA.

17 <sup>3</sup>Department of Pharmaceutical Chemistry, University of California at San Francisco, San  
18 Francisco, CA, USA.

19 <sup>4</sup>Quantitative Biosciences Institute (QBI) Coronavirus Research Group Structural Biology  
20 Consortium, University of California, San Francisco, CA, USA.

21 <sup>5</sup>Department of Cellular and Molecular Pharmacology, University of California at San Francisco,  
22 San Francisco, CA, USA.

23 <sup>6</sup>Viral Populations and Pathogenesis Unit, CNRS UMR 3569, Institut Pasteur, 75724, Paris,  
24 cedex 15, France

25 <sup>7</sup>Department of Pulmonary, Critical Care, Allergy and Sleep Medicine, University of California  
26 San Francisco, San Francisco, CA 94158, USA.

27 <sup>8</sup>Cytiva Life Sciences, Marlborough, MA, USA.

28 <sup>9</sup>Molecular Biophysics and Integrated Bioimaging and the Molecular Foundry, Lawrence  
29 Berkeley National Laboratory, Berkeley, CA, USA.

30 <sup>10</sup>Quantitative Biosciences Institute (QBI), University of California San Francisco, San  
31 Francisco, CA, USA.

32 <sup>11</sup>J. David Gladstone Institutes, San Francisco, CA, USA.

33 <sup>12</sup>Department of Medicine, University of California San Francisco, San Francisco, CA, USA.

34 <sup>13</sup>Department of Microbiology, Icahn School of Medicine at Mount Sinai, New York, NY, USA.

35 <sup>14</sup>Global Health and Emerging Pathogens Institute, Icahn School of Medicine at Mount Sinai,  
36 New York, NY, USA.

37 <sup>15</sup>Department of Anesthesia and Perioperative Care, University of California at San Francisco,  
38 San Francisco, CA, USA.

39

40 # These authors contributed equally

41 \* To whom correspondence should be addressed; Email: [michael@walterlab.ucsf.edu](mailto:michael@walterlab.ucsf.edu),  
42 [peter@walterlab.ucsf.edu](mailto:peter@walterlab.ucsf.edu), [Aashish.Manglik@ucsf.edu](mailto:Aashish.Manglik@ucsf.edu)

43 **Abstract**

44 Without an effective prophylactic solution, infections from SARS-CoV-2 continue to rise  
45 worldwide with devastating health and economic costs. SARS-CoV-2 gains entry into host cells  
46 via an interaction between its Spike protein and the host cell receptor angiotensin converting  
47 enzyme 2 (ACE2). Disruption of this interaction confers potent neutralization of viral entry,  
48 providing an avenue for vaccine design and for therapeutic antibodies. Here, we develop single-  
49 domain antibodies (nanobodies) that potently disrupt the interaction between the SARS-CoV-2  
50 Spike and ACE2. By screening a yeast surface-displayed library of synthetic nanobody  
51 sequences, we identified a panel of nanobodies that bind to multiple epitopes on Spike and  
52 block ACE2 interaction via two distinct mechanisms. Cryogenic electron microscopy (cryo-EM)  
53 revealed that one exceptionally stable nanobody, Nb6, binds Spike in a fully inactive  
54 conformation with its receptor binding domains (RBDs) locked into their inaccessible down-  
55 state, incapable of binding ACE2. Affinity maturation and structure-guided design of  
56 multivalency yielded a trivalent nanobody, mNb6-tri, with femtomolar affinity for SARS-CoV-2  
57 Spike and picomolar neutralization of SARS-CoV-2 infection. mNb6-tri retains stability and  
58 function after aerosolization, lyophilization, and heat treatment. These properties may enable  
59 aerosol-mediated delivery of this potent neutralizer directly to the airway epithelia, promising to  
60 yield a widely deployable, patient-friendly prophylactic and/or early infection therapeutic agent to  
61 stem the worst pandemic in a century.

## 62 **Introduction**

63 Over the last two decades, three zoonotic  $\beta$ -coronaviruses have entered the human population,  
64 causing severe respiratory symptoms with high mortality [1-3]. The ongoing COVID-19  
65 pandemic is caused by SARS-CoV-2, the most readily transmissible of these three  
66 coronaviruses [4-7]. SARS-CoV-2 has wrecked the world's economy and societies to an  
67 unprecedented extent, to date (Aug. 3, 2020) causing 691,320 reported deaths around the  
68 globe [8]. Although public health measures have slowed its spread in many regions, infection  
69 hotspots keep reemerging. No successful vaccine or preventive treatment has yet been  
70 manufactured for any coronavirus, and the time to develop an effective and broadly available  
71 vaccine for SARS-CoV-2 remains uncertain. The development of novel therapeutic and  
72 prophylactic approaches thus remains essential, both as temporary stopgaps until an effective  
73 vaccine is generated and as permanent solutions for those segments of the population for which  
74 vaccination proves ineffective or contraindicated.

75  
76 Coronavirus virions are bounded by a membrane envelope that contains ~25 copies of the  
77 homotrimeric transmembrane spike glycoprotein (Spike) responsible for virus entry into the host  
78 cell [9]. The surface-exposed portion of Spike is composed of two domains, S<sub>1</sub> and S<sub>2</sub> [10]. The  
79 S<sub>1</sub> domain mediates the interaction between virus and its host cell receptor, the angiotensin  
80 converting enzyme 2 (ACE2), while the S<sub>2</sub> domain catalyzes fusion of the viral and host cell  
81 membranes [3, 11-13]. During its biogenesis, the Spike protein is proteolytically cleaved  
82 between the S<sub>1</sub> and S<sub>2</sub> domains, which primes the virus for cellular entry [10]. Contained within  
83 S<sub>1</sub> is the receptor binding domain (RBD), which directly binds to ACE2. The RBD is attached to  
84 the body of Spike by a flexible region and can exist in an inaccessible down-state or an  
85 accessible up-state [14, 15]. Binding to ACE2 requires the RBD in the up-state and enables  
86 cleavage by host proteases TMPRSS2 or cathepsin, triggering a dramatic conformational  
87 change in S<sub>2</sub> that enables viral entry [16]. In SARS-CoV-2 virions, Spike oscillates between an  
88 active, open conformation with at least one RBD in the up-state and an inactive, closed  
89 conformation with all RBDs in the down-state [9, 11, 14, 15].

90  
91 By screening a high-complexity yeast surface-displayed library of synthetic nanobodies, we  
92 have uncovered a collection of nanobodies that block the Spike-ACE2 interaction. Biochemical  
93 and structural studies revealed that two classes of these nanobodies act in distinct ways to  
94 prevent ACE2 binding. Combining affinity maturation and structure-guided multimerization, we  
95 optimized these agents and generated Spike binders that match or exceed the potency of most

96 monoclonal antibodies disclosed to date. Our lead neutralizing molecule, mNb6-tri, blocks  
97 SARS-CoV-2 entry in human cells at picomolar efficacy and withstands aerosolization,  
98 lyophilization, and elevated temperatures. mNb6-tri provides a promising approach to deliver a  
99 potent SARS-CoV-2 neutralizing molecule directly to the airways for prophylaxis or therapy.

100

## 101 **Results**

### 102 **Synthetic nanobodies that disrupt Spike-ACE2 interaction**

103 To isolate nanobodies that neutralize SARS-CoV-2, we screened a yeast surface-displayed  
104 library of  $>2 \times 10^9$  synthetic nanobody sequences. Our strategy was to screen for binders to the  
105 full Spike protein ectodomain, in order to capture not only those nanobodies that would compete  
106 by binding to the ACE2-binding site on the RBD directly but also those that might bind  
107 elsewhere on Spike and block ACE2 interaction through indirect mechanisms. We used a  
108 mutant form of SARS-CoV-2 Spike, Spike\*, as the antigen [15]. Spike\* lacks one of the two  
109 activating proteolytic cleavage sites between the S<sub>1</sub> and S<sub>2</sub> domains and introduces two  
110 mutations to stabilize the pre-fusion conformation. Spike\* expressed in mammalian cells binds  
111 ACE2 with a  $K_D = 44$  nM (Supplementary Fig. 1), consistent with previous reports [17]. Next, we  
112 labeled Spike\* with biotin or with fluorescent dyes and selected nanobody-displaying yeast over  
113 multiple rounds, first by magnetic bead binding and then by fluorescence-activated cell sorting  
114 (Fig. 1A).

115

116 Three rounds of selection yielded 21 unique nanobodies that bound Spike\* and showed  
117 decreased Spike\* binding in the presence of ACE2. Closer inspection of their binding properties  
118 revealed that these nanobodies fall into two distinct classes. One group (Class I) binds the RBD  
119 and competes with ACE2 (Fig. 1B). A prototypical example of this class is nanobody Nb6, which  
120 binds to Spike\* and to RBD alone with a  $K_D$  of 210 nM and 41 nM, respectively (Fig. 1C; Table  
121 1). Another group (Class II), exemplified by nanobody Nb3, binds to Spike\* ( $K_D = 61$  nM), but  
122 displays no binding to RBD alone (Fig. 1C, Table 1). In the presence of excess ACE2, binding of  
123 Nb6 and other Class I nanobodies is blocked entirely, whereas binding of Nb3 and other Class II  
124 nanobodies is decreased only moderately (Fig. 1B). These results suggest that Class I  
125 nanobodies target the RBD to block ACE2 binding, whereas Class II nanobodies target other  
126 epitopes and decrease ACE2 interaction with Spike allosterically or through steric interference.  
127 Indeed, surface plasmon resonance (SPR) experiments demonstrate that Class I and Class II  
128 nanobodies can bind Spike\* simultaneously (Fig. 1D).

129

130 Analysis of the kinetic rate constants for Class I nanobodies revealed a consistently greater  
131 association rate constant ( $k_a$ ) for nanobody binding to the isolated RBD than to full-length Spike\*  
132 (Table 1), which suggests that RBD accessibility influences the  $K_D$ . We next tested the efficacy  
133 of our nanobodies, both Class I and Class II, to inhibit binding of fluorescently labeled Spike\* to  
134 ACE2-expressing HEK293 cells (Table 1, Fig. 1E). Class I nanobodies emerged with highly  
135 variable activity in this assay with Nb6 and Nb11 as two of the most potent clones with  $IC_{50}$   
136 values of 370 and 540 nM, respectively (Table 1). For unexplained reasons, Class II nanobodies  
137 showed little to no activity in this assay (Table 1, Fig. 1E).

138

139 Going forward, we prioritized two Class I nanobodies, Nb6 and Nb11, that combine potent  
140 Spike\* binding with relatively small differences in  $k_a$  between binding to Spike\* or RBD. We  
141 reasoned that the epitopes recognized by Nb6 and Nb11 would be more readily accessible in  
142 the Spike protein on intact virions. For Class II nanobodies we prioritized Nb3 because of its  
143 optimal stability and yield during purification.

144

#### 145 **Nb6 and Nb11 target the RBD and directly compete with ACE2**

146 To define the binding sites of Nb6 and Nb11, we determined their cryogenic electron  
147 microscopy (cryo-EM) structures bound to Spike\* (Fig. 2A-B, Supplementary Fig. 2-4,  
148 Supplementary Table 1). Both nanobodies recognize RBD epitopes that overlap the ACE2  
149 binding site (Fig. 2E). For Nb6 and Nb11, we resolved nanobody binding to both the open and  
150 closed conformations of Spike\*. We obtained a 3.0 Å map of Nb6 bound to closed Spike\*, which  
151 enabled modeling of the Nb6-Spike\* complex (Fig. 2A), including the complementarity  
152 determining regions (CDRs). We also obtained lower resolution maps for Nb6 bound to open  
153 Spike\* (3.8 Å), Nb11 bound to open Spike\* (4.2 Å), and Nb11 bound to closed Spike\* (3.7 Å).  
154 For these lower resolution maps, we could define the nanobody's binding orientation but not  
155 accurately model the CDRs.

156

157 Nb6 bound to closed Spike\* straddles the interface between two adjacent RBDs. The majority of  
158 the contacting surfaces are contributed by CDR1 and CDR2 of Nb6 (Fig. 2C). CDR3 contacts  
159 the adjacent RBD that is counterclockwise positioned when viewed from the top of Spike\* (Fig.  
160 2C). The binding of one Nb6 therefore stabilizes two adjacent RBDs in the down-state. We  
161 surmise that this initial binding event pre-organizes the binding site for a second and third Nb6  
162 molecule to stabilize the closed Spike\* conformation. Indeed, binding of two Nb6 molecules  
163 would lock all three RBDs into the down-state, thus highly favoring binding of a third Nb6

164 because binding would not entail any further entropic cost. By contrast, Nb11 bound to down-  
165 state RBDs only contacts a single RBD (Fig. 2D).

166

### 167 **Nb3 interacts with the Spike S<sub>1</sub> domain external to the RBD**

168 Our attempts to determine the binding site of Nb3 by cryo-EM proved unsuccessful. We  
169 therefore turned to radiolytic hydroxyl radical footprinting to determine potential binding sites for  
170 Nb3. Spike\*, either apo or bound to Nb3, was exposed to 5-50 milliseconds of synchrotron X-ray  
171 radiation to label solvent exposed amino acids with hydroxyl radicals. Radical-labeled amino  
172 acids were subsequently identified and quantified by mass spectrometry of trypsin/Lys-C or Glu-  
173 C protease digested Spike\*[18]. Two neighboring surface residues on the S<sub>1</sub> domain of Spike  
174 (M177 and H207) emerged as highly protected sites in the presence of Nb3 (Supplementary  
175 Fig. 5). The degree of protection is consistent with prior observations of antibody-antigen  
176 interactions by hydroxyl radical footprinting [19]. Both M177 and H207 are greater than 40 Å  
177 distant from the ACE2 binding site on the RBD, suggesting that Nb3 may inhibit Spike-ACE2  
178 interactions through allosteric means.

179

### 180 **Rationally engineered multivalency increases potency**

181 The structure of Nb6 bound to closed Spike\* enabled us to engineer bivalent and trivalent  
182 nanobodies predicted to lock all RBDs in the down-state. To this end, we inserted flexible Gly-  
183 Ser linkers of either 15 or 20 amino acids to span the 52 Å distance between adjacent Nb6  
184 monomers bound to down-state RBDs in closed Spike\* (Supplementary Fig. 6). Both linker  
185 lengths are too short to span the distance (72 Å) between Nb6 bound to a down-state RBD and  
186 an up-state RBD that would co-exist in an open Spike. Moreover, binding of three RBDs in the  
187 previously reported conformation of Nb6-bound open Spike\* would be physically impossible  
188 even with longer linker length because of steric clashes (Supplementary Fig. 6). By contrast, the  
189 minimum distance between adjacent Nb11 monomers bound to either open or closed Spike\* is  
190 68 Å (Supplementary Fig. 6). We therefore predicted that multivalent binding by Nb6 constructs  
191 would display significantly slowed dissociation rates due to the enhanced avidity afforded by  
192 Spike's trimeric architecture.

193

194 We assessed multivalent Nb6 binding to Spike\* by SPR. Both bivalent Nb6 with a 15 amino acid  
195 linker (Nb6-bi) and trivalent Nb6 with two 20 amino acid linkers (Nb6-tri) dissociate from Spike\*  
196 in a biphasic manner. The dissociation phase can be fitted to two components: a fast phase with  
197 kinetic rate constants  $k_{d1}$  of  $2.7 \times 10^{-2} \text{ s}^{-1}$  for Nb6-bi and  $2.9 \times 10^{-2} \text{ s}^{-1}$  for Nb6-tri, which are of the

198 same magnitude as that observed for monovalent Nb6 ( $k_d = 5.6 \times 10^{-2} \text{ s}^{-1}$ ) and a slow phase that  
199 is dependent on avidity ( $k_{d2} = 3.1 \times 10^{-4}$  for Nb6-bi and  $k_{d2} < 1.0 \times 10^{-6} \text{ s}^{-1}$  for Nb6-tri, respectively)  
200 (Fig. 3A). The relatively similar  $k_d$  for the fast phase suggests that a fraction of the observed  
201 binding for the multivalent constructs is nanobody binding to a single Spike\* RBD. By contrast,  
202 the slow dissociation phase of Nb6-bi and Nb6-tri indicates engagement of two or three RBDs.  
203 We observed no dissociation for the slow phase of Nb6-tri over 10 minutes, indicating an upper  
204 boundary for  $k_{d2}$  of  $1 \times 10^{-6} \text{ s}^{-1}$  and subpicomolar affinity. This measurement remains an upper-  
205 bound estimate rather than an accurate measurement because the technique is limited by the  
206 intrinsic dissociation rate of Spike\* from the chip imposed by the chemistry used to immobilize  
207 Spike\*.

208

209 We reasoned that the biphasic dissociation behavior could be explained by a slow  
210 interconversion between up- and down-state RBDs, with conversion to the more stable down-  
211 state required for full trivalent binding. According to this view, a single domain of Nb6-tri  
212 engaged with an up-state RBD would dissociate rapidly. The system would then re-equilibrate  
213 as the RBD flips into the down-state, eventually allowing Nb6-tri to trap all RBDs in closed  
214 Spike\*. To test this notion directly, we varied the time allowed for Nb6-tri binding to Spike\*.  
215 Indeed, we observed an exponential decrease in the percent fast-phase with a  $t_{1/2}$  of 65 s (Fig.  
216 3B), which, we surmise, reflects the timescale of conversion between the RBD up- and down-  
217 states in Spike\*. Taken together, dimerization and trimerization of Nb6 afforded 750-fold and  
218 >200,000-fold gains in  $K_D$ , respectively.

219

## 220 **Class I and II nanobodies prevent SARS-CoV-2 infection**

221 We next tested the neutralization activity of trivalent versions of our top Class I (Nb6 and Nb11)  
222 and Class II (Nb3) nanobodies against SARS-CoV-2 pseudotyped lentivirus. In this assay,  
223 SARS-CoV-2 Spike is expressed as a surface protein on a lentiviral particle that contains a  
224 ZsGreen reporter gene, which is integrated and expressed upon successful viral entry into cells  
225 harboring the ACE2 receptor [20]. Nb6 and Nb11 inhibited pseudovirus infection with  $IC_{50}$   
226 values of 2.0  $\mu\text{M}$  and 2.4  $\mu\text{M}$ , respectively, and Nb3 inhibited pseudovirus infection with an  $IC_{50}$   
227 of 3.9  $\mu\text{M}$  (Fig. 3C, Table 1). Nb6-tri shows a 2000-fold enhancement of inhibitory activity, with  
228 an  $IC_{50}$  of 1.2 nM, whereas trimerization of Nb11 and Nb3 resulted in more modest gains of 40-  
229 and 10-fold (51 nM and 400 nM), respectively (Fig. 3C).

230



231 We next confirmed these neutralization activities with a viral plaque assay using live SARS-  
232 CoV-2 virus infection of VeroE6 cells. Consistent with its activity against pseudotyped lentivirus,  
233 Nb6-tri proved exceptionally potent, neutralizing SARS-CoV-2 with an average IC<sub>50</sub> of 160 pM  
234 (Fig. 3D). Nb3-tri neutralized SARS-CoV-2 with an average IC<sub>50</sub> of 140 nM (Fig. 3D).

235

### 236 **Affinity maturation yields a femtomolar K<sub>D</sub> Spike inhibitor**

237 We further optimized the potency of Nb6 by selecting high-affinity variants. To this end, we  
238 prepared a new library, starting with the Nb6 coding sequence, in which we varied each amino  
239 acid position of all three CDRs by saturation mutagenesis (Fig. 4A). After two rounds of  
240 magnetic bead-based selection, we isolated a population of high-affinity clones. Sequencing  
241 revealed two highly penetrant mutations: I27Y in CDR1 and P105Y in CDR3. We incorporated  
242 these two mutations into Nb6 to generate matured Nb6 (mNb6), which binds with 500-fold  
243 increased affinity to Spike\* as measured by SPR (Fig. 4B). As a monomer, mNb6 inhibits both  
244 pseudovirus and live SARS-CoV-2 infection with low nanomolar potency, a ~200-fold  
245 improvement compared to Nb6 (Fig. 4I-J, Table 1).

246

247 A 2.9 Å cryo-EM structure of mNb6 bound to Spike\* shows that, like the parent nanobody Nb6,  
248 mNb6 binds to closed Spike (Fig. 4C, Supplementary Fig. 7). The higher resolution map allowed  
249 us to build a model with high confidence and determine the effects of the I27Y and P105Y  
250 substitutions. mNb6 induces a slight rearrangement of the down-state RBDs as compared to  
251 both previously determined structures of apo-Spike\* and Spike\* bound to Nb6, inducing a 9°  
252 rotation of the RBD away from the central three-fold symmetry axis (Fig. 4H) [14, 15]. This  
253 deviation likely arises from a different interaction between CDR3 and Spike\*, which nudges the  
254 RBDs into a new resting position. While the I27Y substitution optimizes local contacts between  
255 CDR1 in its original binding site on the RBD, the P105Y substitution leads to a marked  
256 rearrangement of CDR3 in mNb6 (Fig. 4F-G). This conformational change yields a different set  
257 of contacts between mNb6 CDR3 and the adjacent RBD (Fig. 4D). Remarkably, an X-ray crystal  
258 structure of mNb6 alone revealed dramatic conformational differences in CDR1 and CDR3  
259 between free and Spike\*-bound mNb6, suggestive of significant conformational heterogeneity  
260 for the unbound nanobodies and induced-fit rearrangements upon binding to Spike\* (Fig. 4E).

261

262 The binding orientation of mNb6 is similar to that of Nb6, supporting the notion that our  
263 multivalent design would likewise enhance binding affinity. Unlike Nb6-tri, trivalent mNb6  
264 (mNb6-tri) bound to Spike with no observable fast-phase dissociation and no measurable

265 dissociation over ten minutes, yielding an upper bound for the dissociation rate constant  $k_d$  of  
266  $1.0 \times 10^{-6} \text{ s}^{-1}$  ( $t_{1/2} > 8$  days) and a  $K_D$  of  $< 1$  pM (Fig. 4B). As above, more precise measurements  
267 of the dissociation rate are precluded by the surface chemistry used to immobilize Spike\*.

268

269 mNb6-tri displays further gains in potency in both pseudovirus and live SARS-CoV-2 infection  
270 assays with  $IC_{50}$  values of 120 pM (5.0 ng/mL) and 54 pM (2.3 ng/mL), respectively (Fig. 4H-I,  
271 Table 1). Given the sub-picomolar affinity observed by SPR, it is likely that these viral  
272 neutralization potencies reflect the lower limit of the assays. mNb6-tri is therefore an  
273 exceptionally potent SARS-CoV-2 neutralizing antibody, among the most potent molecules  
274 disclosed to date.

275

### 276 **Nb6, Nb6-tri, mNb6, and mNb6-tri are robust proteins**

277 One of the most attractive properties that distinguishes nanobodies from traditional monoclonal  
278 antibodies is their extreme stability [21]. We therefore tested Nb6, Nb6-tri, mNb6, and mNb6-tri  
279 for stability regarding temperature, lyophilization, and aerosolization. Temperature denaturation  
280 experiments using circular dichroism measurements to assess protein unfolding revealed  
281 melting temperatures of 66.9, 62.0, 67.6, and 61.4 °C for Nb6, Nb6-tri, mNb6 and mNb6-tri,  
282 respectively (Fig 5A). Aerosolization and prolonged heating of Nb6, mNb6, and mNb6-tri for 1  
283 hour at 50°C induced no loss of activity (Fig 5B). Moreover, mNb6 and mNb6-tri were stable to  
284 lyophilization and to aerosolization using a mesh nebulizer, showing no aggregation by size  
285 exclusion chromatography and preserved high affinity binding to Spike\* (Fig. 5C-D).

286

### 287 **Discussion**

288 There is a pressing need for prophylactics and therapeutics against SARS-CoV-2 infection.  
289 Most recent strategies to prevent SARS-CoV-2 entry into the host cell aim at blocking the  
290 ACE2-RBD interaction. High-affinity monoclonal antibodies, many identified from convalescent  
291 patients, are leading the way as potential therapeutics [22-29]. While highly effective *in vitro*,  
292 these agents are expensive to produce by mammalian cell expression and need to be  
293 intravenously administered by healthcare professionals. Moreover, large doses are likely to be  
294 required for prophylactic viral neutralization, as only a small fraction of systemically circulating  
295 antibodies cross the epithelial cell layers that line the airways [30]. By contrast, single domain  
296 antibodies (nanobodies) provide significant advantages in terms of production and deliverability.  
297 They can be inexpensively produced at scale in bacteria (*E. coli*) or yeast (*P. pastoris*).

298 Furthermore, their inherent stability enables aerosolized delivery directly to the nasal and lung  
299 epithelia by self-administered inhalation [31].

300

301 Monomeric mNb6 is among the most potent single domain antibodies neutralizing SARS-CoV-2  
302 discovered to date. Multimerization of single domain antibodies has been shown to improve  
303 target affinity by avidity [31, 32]. In the case of Nb6 and mNb6, however, our design strategy  
304 enabled a multimeric construct that simultaneously engages all three RBDs, yielding profound  
305 gains in potency. Furthermore, because RBDs must be in the up-state to engage with ACE2,  
306 conformational control of RBD accessibility can serve as an added neutralization mechanism.  
307 Indeed, our Nb6-tri and mNb6-tri molecules were designed with this functionality in mind. Thus,  
308 when mNb6-tri engages with Spike, it prevents ACE2 binding by both directly occluding the  
309 binding site and by locking the RBDs into an inactive conformation. Although a multitude of  
310 other monoclonal and single-domain antibodies against SARS-CoV-2 Spike have been  
311 discovered to date, there are few if any molecules as potent and stable as mNb6-tri [32-42].  
312 Resistance to aerosolization, in particular, offers unprecedented opportunity for patient-friendly  
313 nasal and pulmonary administration.

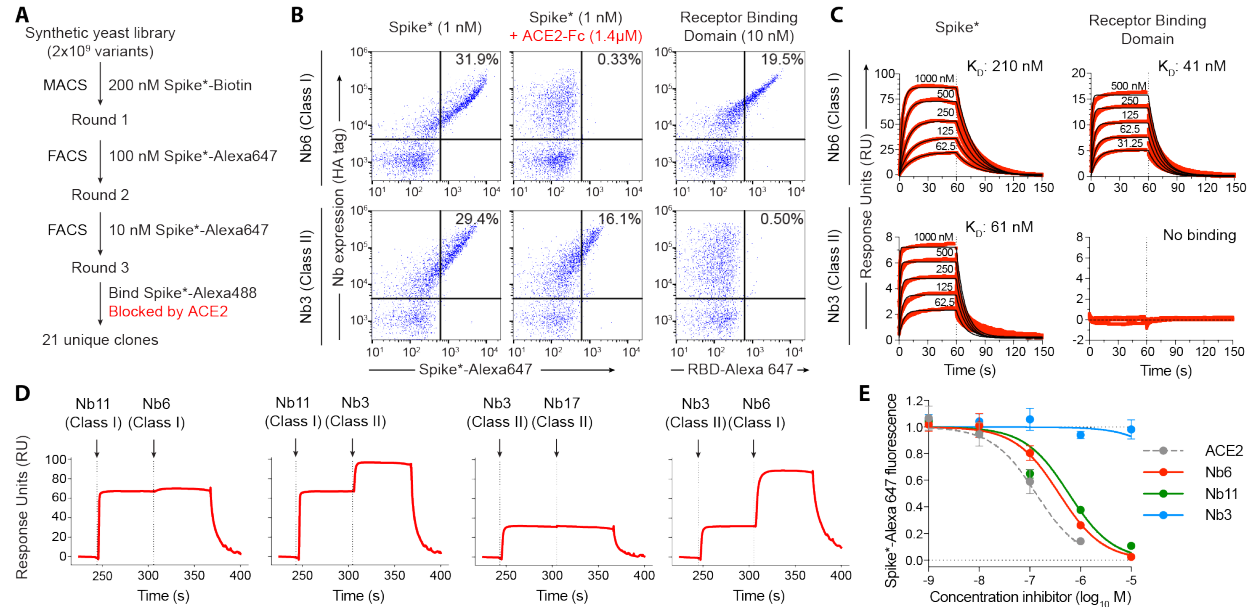
314

315 Our discovery of Class II neutralizing nanobodies demonstrates the presence of previously  
316 unexplored mechanisms of blocking Spike binding to ACE2. For one Class II nanobody, Nb3,  
317 we identified a likely binding site in the Spike S<sub>1</sub> domain external to the RBDs. Previously  
318 discovered neutralizing antibodies from convalescent patients bind an epitope in a similar region  
319 of Spike [24, 26, 27]. Binding of Nb3 to this epitope may allosterically stabilize RBDs in the  
320 down-state, thereby decreasing ACE2 binding. Pairing of Class I and Class II nanobodies in a  
321 prophylactic or therapeutic cocktail could thus be a highly advantageous strategy for both potent  
322 neutralization and prevention of escape variants. The combined stability, potency, and diverse  
323 epitope engagement of our anti-Spike nanobodies therefore provide a unique potential  
324 prophylactic and therapeutic strategy to limit the continued toll of the COVID-19 pandemic.

325

326 **MAIN TEXT FIGURES**

**Figure 1**



327

328

329 **Figure 1. Discovery of two distinct classes of anti-Spike nanobodies.** **A**, Selection strategy

330 for identification of anti-Spike nanobodies that disrupt Spike-ACE2 interactions using magnetic

331 bead selections (MACS) or fluorescence activated cell sorting (FACS). **B**, Flow cytometry of

332 yeast displaying Nb6 (a Class I nanobody) or Nb3 (a Class II nanobody). Nb6 binds Spike\*-

333 Alexa 647 and receptor binding domain (RBD-Alexa 647). Nb6 binding to Spike\* is completely

334 disrupted by an excess (1.4 μM) of ACE2-Fc. Nb3 binds Spike\*, but not the RBD. Nb3 binding

335 to Spike\* is partially decreased by ACE2-Fc. **C**, SPR of Nb6 and Nb3 binding to either Spike\* or

336 RBD. Red traces are raw data and global kinetic fits are shown in black. Nb3 shows no binding

337 to RBD. **D**, SPR experiments with immobilized Spike\* show that Class I and Class II nanobodies

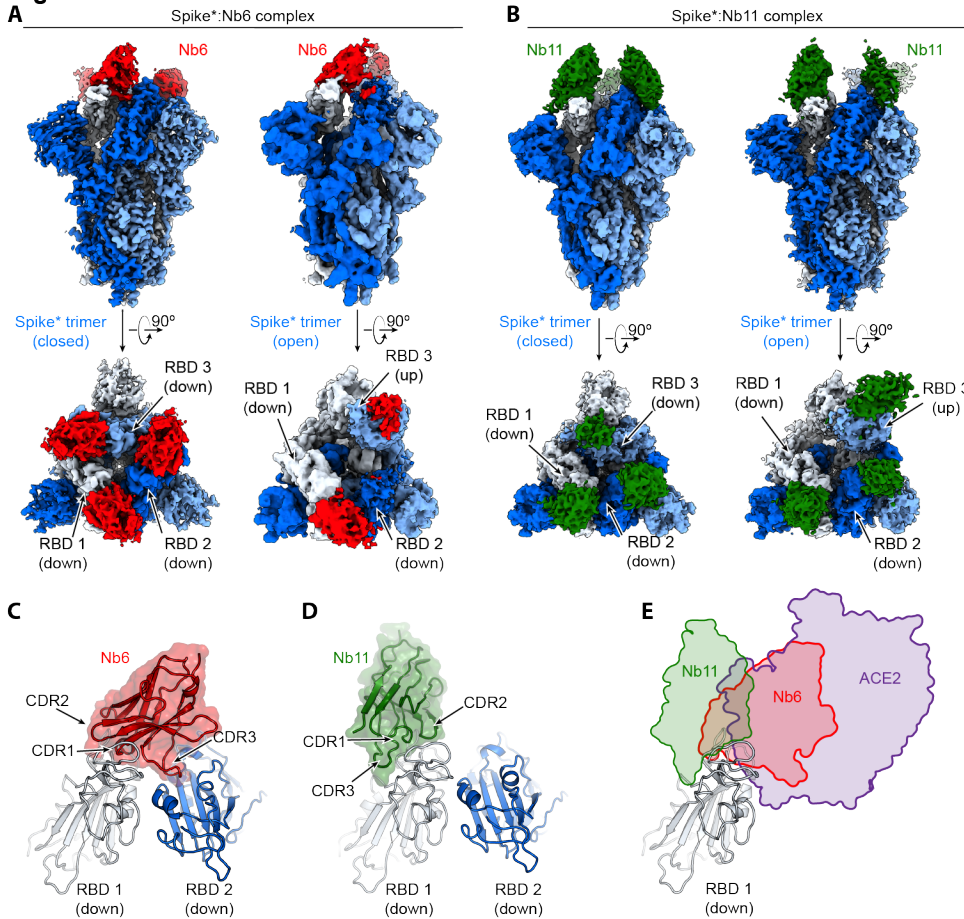
338 can bind Spike\* simultaneously. By contrast, two Class I nanobodies or Class II nanobodies do

339 not bind simultaneously. **E**, Nanobody inhibition of 1 nM Spike\*-Alexa 647 binding to ACE2

340 expressing HEK293T cells. n = 3 (ACE2, Nb3) or 5 (Nb6, Nb11) biological replicates. All error

341 bars represent s.e.m.

**Figure 2**



342

343

344 **Figure 2. Cryo-EM structures of Nb6 and Nb11 bound to Spike. A, Cryo-EM maps of Spike\*-**

345 **Nb6 complex in either closed (left) or open (right) Spike\* conformation. B, Cryo-EM maps of**

346 **Spike\*-Nb11 complex in either closed (left) or open (right) Spike\* conformation. The top views**

347 **show receptor binding domain (RBD) up- or down-states. C, Nb6 straddles the interface of two**

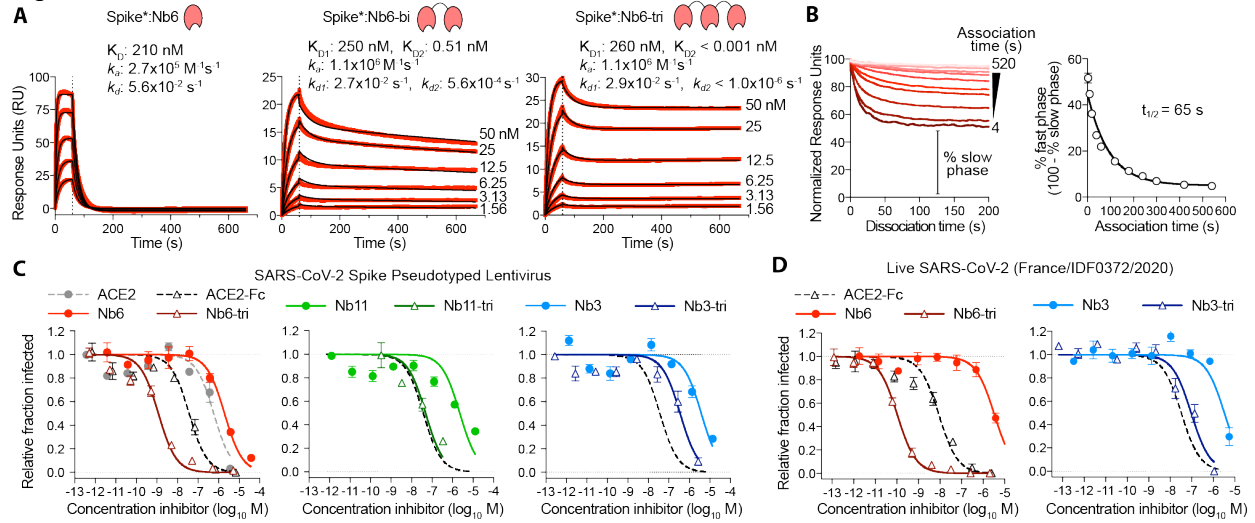
348 **down-state RBDs, with CDR3 reaching over to an adjacent RBD. D, Nb11 binds a single RBD in**

349 **the down-state (displayed) or similarly in the up-state. No cross-RBD contacts are made by**

350 **Nb11 in either RBD up- or down-state. E, Comparison of RBD epitopes engaged by ACE2**

351 **(purple), Nb6 (red), or Nb11 (green). Both Nb11 and Nb6 directly compete with ACE2 binding.**

**Figure 3**



352

353

354 **Figure 3. Multivalency improves nanobody affinity and inhibitory efficacy. A**, SPR of Nb6

355 and multivalent variants. Red traces show raw data and black lines show global kinetic fit for

356 Nb6 and independent fits for association and dissociation phases for Nb6-bi and Nb6-tri. **B**,

357 Dissociation phase SPR traces for Nb6-tri after variable association time ranging from 4 to 520

358 s. Curves were normalized to maximal signal at the beginning of the dissociation phase. Percent

359 fast phase is plotted as a function of association time (right) with a single exponential fit.  $n = 3$

360 independent biological replicates. **C**, Inhibition of pseudotyped lentivirus infection of ACE2

361 expressing HEK293T cells.  $n = 3$  biological replicates for all but Nb11-tri ( $n = 2$ ) **D**, Inhibition of

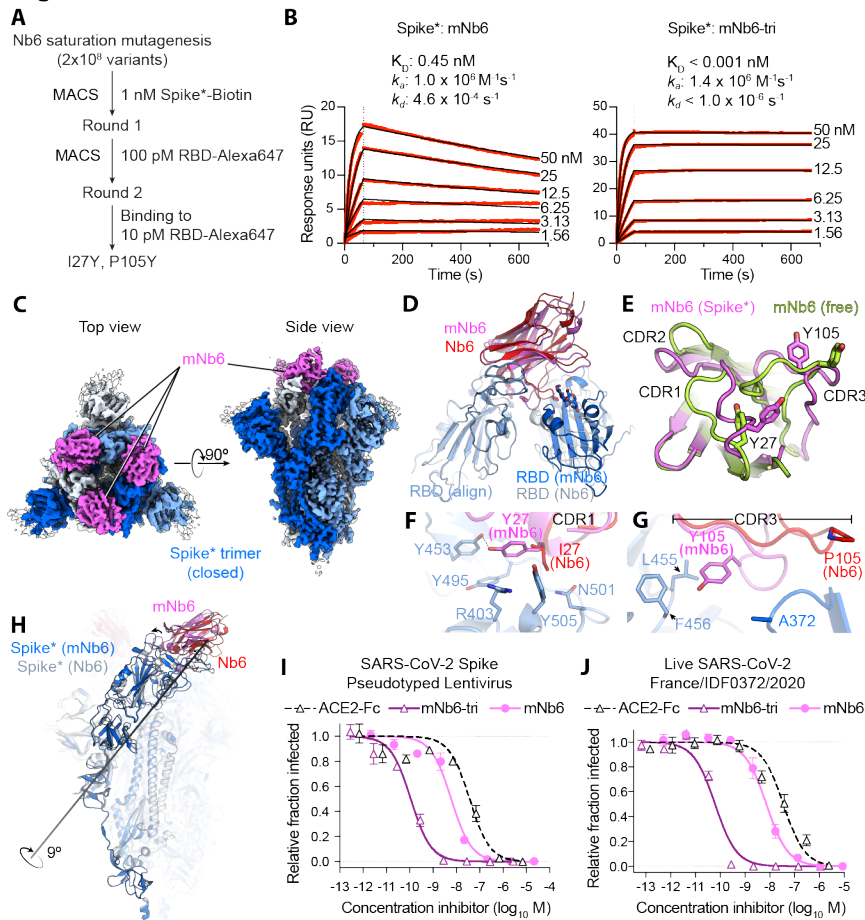
362 live SARS-CoV-2 virus. Representative biological replicate with  $n = 3$  (right panel) or 4 (left

363 panel) technical replicates per concentration.  $n = 3$  biological replicates for all but Nb3 and Nb3-

364 tri ( $n = 2$ ). All error bars represent s.e.m.

365

**Figure 4**



366

367

368 **Figure 4. Affinity maturation of Nb6 yields a picomolar SARS-CoV-2 neutralizing**

369 **molecule. A**, A saturation mutagenesis library of Nb6 was subjected to two rounds of selection

370 to identify consensus mutations I27Y and P105Y. **B**, SPR of mNb6 and mNb6-tri binding to

371 immobilized Spike\*. Red traces show raw data and black lines show global kinetic fit. No

372 dissociation was observed for mNb6-tri over 10 minutes. **C**, Cryo-EM structure of Spike\*-mNb6

373 complex. **D**, Comparison of receptor binding domain (RBD) engagement by Nb6 and mNb6.

374 One RBD was used to align both structures (RBD align), demonstrating changes in Nb6 and

375 mNb6 position and the adjacent RBD. **E**, Comparison of mNb6 complementarity determining

376 regions in either the cryo-EM structure of the Spike\*-mNb6 complex or an X-ray crystal structure

377 of mNb6 alone. **F**, CDR1 of Nb6 and mNb6 binding to the RBD. As compared to I27 in Nb6, Y27

378 of mNb6 hydrogen bonds to Y453 and optimizes pi-pi and pi-cation interactions with the RBD.

379 **G**, CDR3 of Nb6 and mNb6 binding to the RBD demonstrating a large conformational

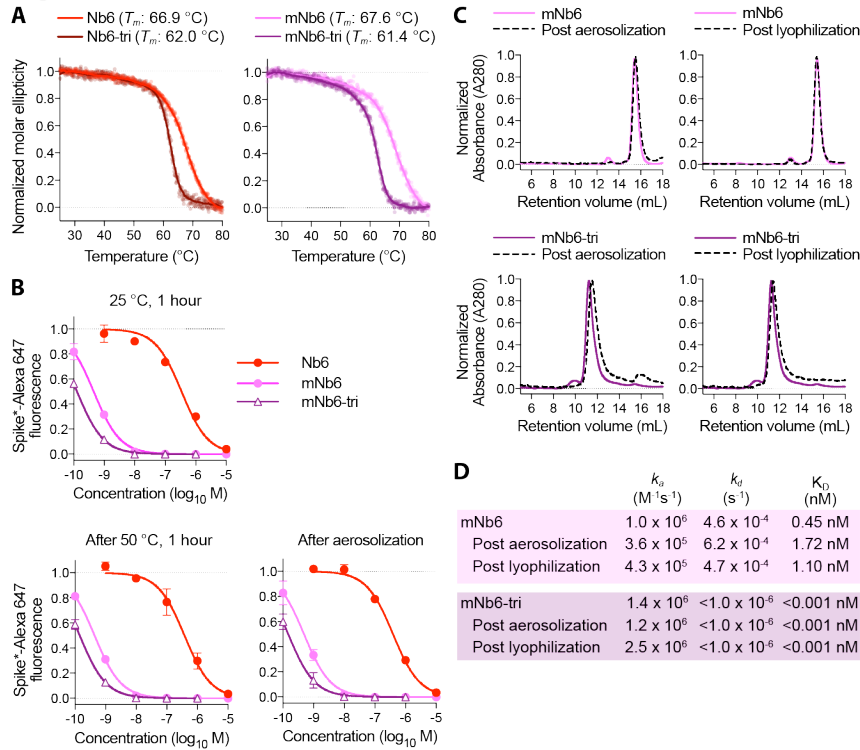
380 rearrangement of the entire loop in mNb6. **H**, Comparison of closed Spike\* bound to mNb6 and

381 Nb6. Rotational axis for RBD movement is highlighted. **I**, Inhibition of pseudotyped lentivirus

382 infection of ACE2 expressing HEK293T cells by mNb6 and mNb6-tri. n = 3 biological replicates  
383 **J**, mNb6 and mNb6-tri inhibit SARS-CoV-2 infection of VeroE6 cells in a plaque assay.  
384 Representative biological replicate with n = 4 technical replicates per concentration. n = 3  
385 biological replicates for all samples. All error bars represent s.e.m.  
386



**Figure 5**



387

388 **Figure 5. Nb6 and its derivatives are robust proteins. A,** Thermal denaturation of nanobodies

389 assessed by circular dichroism measurement of molar ellipticity at 204 nm. Apparent melting

390 temperatures ( $T_m$ ) for each nanobody are indicated. **B,** Nanobody inhibition of 1 nM Spike\*-

391 Alexa 647 binding to ACE2 expressing HEK293T cells after incubation at either 25 °C or 50 °C

392 for 1 hour or after aerosolization. **C,** Size exclusion chromatography of nanobodies after

393 lyophilization or aerosolization. **D,** Summary table of SPR kinetics data and affinities for

394 aerosolized or lyophilized mNb6 and mNb6-tri.

395

396 **Table 1. Anti-Spike nanobody affinity and neutralization potency**

Nanobody	Class	Spike* Binding			RBD Binding			Spike* Competition IC <sub>50</sub> (s.e.m) (M) <sup>a</sup>	SARS-CoV-2 Pseudovirus IC <sub>50</sub> (s.e.m.) (M) <sup>b</sup>	Live SARS-CoV-2 IC <sub>50</sub> (s.e.m.) (M) <sup>c</sup>
		k <sub>a</sub> (M <sup>-1</sup> s <sup>-1</sup> )	k <sub>d</sub> (s <sup>-1</sup> )	K <sub>D</sub> (M)	k <sub>a</sub> (M <sup>-1</sup> s <sup>-1</sup> )	k <sub>d</sub> (s <sup>-1</sup> )	K <sub>D</sub> (M)			
Nb2	I	9.0x10 <sup>5</sup>	5.3x10 <sup>-1</sup>	5.9x10 <sup>-7</sup>	1.0x10 <sup>6</sup>	9.9x10 <sup>-1</sup>	9.7x10 <sup>-7</sup>	8.3x10 <sup>-6</sup> (1.7x10 <sup>-6</sup> )	NP	NP
Nb3	II	1.8x10 <sup>6</sup>	1.1x10 <sup>-1</sup>	6.1x10 <sup>-8</sup>	NB			NC	3.9x10 <sup>-6</sup> (7.9x10 <sup>-7</sup> )	3.0x10 <sup>-6</sup> (3.2x10 <sup>-7</sup> )
Nb6	I	2.7x10 <sup>5</sup>	5.6x10 <sup>-2</sup>	2.1x10 <sup>-7</sup>	2.1x10 <sup>6</sup>	8.7x10 <sup>-2</sup>	4.1x10 <sup>-8</sup>	3.7x10 <sup>-7</sup> (4.9x10 <sup>-8</sup> )	2.0x10 <sup>-6</sup> (3.5x10 <sup>-7</sup> )	3.3x10 <sup>-6</sup> (7.2x10 <sup>-7</sup> )
Nb8	I	1.4x10 <sup>5</sup>	8.1x10 <sup>-1</sup>	5.8x10 <sup>-6</sup>	6.6x10 <sup>5</sup>	3.3x10 <sup>-1</sup>	5.1x10 <sup>-7</sup>	4.8x10 <sup>-6</sup> (4.9x10 <sup>-7</sup> )	NP	NP
Nb11	I	1.2x10 <sup>6</sup>	1.6x10 <sup>-1</sup>	1.4x10 <sup>-7</sup>	3.2x10 <sup>6</sup>	2.4x10 <sup>-1</sup>	7.6x10 <sup>-8</sup>	5.4x10 <sup>-7</sup> (1.2x10 <sup>-7</sup> )	2.4x10 <sup>-6</sup> (5.4x10 <sup>-7</sup> )	NP
Nb12	I	1.2x10 <sup>2</sup>	2.0x10 <sup>-4</sup>	1.6x10 <sup>-6</sup>	Biphasic	Biphasic	Biphasic	2.5x10 <sup>-7</sup> (5.5x10 <sup>-8</sup> )	1.2x10 <sup>-6</sup> (9.0x10 <sup>-7</sup> )	NP
Nb15	I	1.7x10 <sup>5</sup>	2.3x10 <sup>-1</sup>	1.3x10 <sup>-6</sup>	6.0x10 <sup>5</sup>	2.2x10 <sup>-1</sup>	3.6x10 <sup>-7</sup>	2.2x10 <sup>-6</sup> (2.5x10 <sup>-7</sup> )	6.7x10 <sup>-6</sup> (3.6x10 <sup>-6</sup> )	NP
Nb16	I	1.1x10 <sup>5</sup>	1.3x10 <sup>-1</sup>	1.3x10 <sup>-6</sup>	NP			9.5x10 <sup>-7</sup> (1.1x10 <sup>-7</sup> )	NP	NP
Nb17	II	7.3x10 <sup>5</sup>	2.0x10 <sup>-1</sup>	2.7x10 <sup>-7</sup>	NB			NC	7.6x10 <sup>-6</sup> (1.0x10 <sup>-6</sup> )	NP
Nb18	II	1.4x10 <sup>5</sup>	6.4x10 <sup>-3</sup>	4.5x10 <sup>-8</sup>	NB			5.2x10 <sup>-5</sup> (1.5x10 <sup>-5</sup> )	NP	NP
Nb19	I	2.4x10 <sup>4</sup>	1.1x10 <sup>-1</sup>	4.5x10 <sup>-6</sup>	1.0x10 <sup>5</sup>	8.9x10 <sup>-2</sup>	8.8x10 <sup>-7</sup>	4.1x10 <sup>-6</sup> (4.9x10 <sup>-7</sup> )	2.4x10 <sup>-5</sup> (7.7x10 <sup>-6</sup> )	NP
Nb24	I	9.3x10 <sup>5</sup>	2.7x10 <sup>-1</sup>	2.9x10 <sup>-7</sup>	2.4x10 <sup>6</sup>	3.5x10 <sup>-1</sup>	1.5x10 <sup>-7</sup>	7.5x10 <sup>-7</sup> (1.0x10 <sup>-7</sup> )	NP	NP
ACE2	N/A	2.7x10 <sup>5</sup>	1.2x10 <sup>-2</sup>	4.4x10 <sup>-8</sup>	NP	NP	NP	1.7x10 <sup>-7</sup> (6.6x10 <sup>-8</sup> )	6.2x10 <sup>-7</sup> (1.7x10 <sup>-7</sup> )	NP
mNb6	I	1.0x10 <sup>6</sup>	4.5x10 <sup>-4</sup>	4.5x10 <sup>-10</sup>	1.1x10 <sup>6</sup>	6.4x10 <sup>-4</sup>	5.6x10 <sup>-10</sup>	1.3x10 <sup>-9</sup> (4.1x10 <sup>-10</sup> )	6.3x10 <sup>-9</sup> (1.6x10 <sup>-9</sup> )	1.2x10 <sup>-8</sup> (2.5x10 <sup>-9</sup> )
Nb3-bi	II	NP	NP	NP	NP	NP	NP	NP	3.6x10 <sup>-7</sup> (1.5x10 <sup>-7</sup> )	1.8x10 <sup>-7</sup> (1.2x10 <sup>-8</sup> )
Nb3-tri	II	Biphasic	Biphasic	Biphasic	NP	NP	NP	4.1x10 <sup>-8</sup> (1.6x10 <sup>-8</sup> )	4.0x10 <sup>-7</sup> (1.6x10 <sup>-7</sup> )	1.4x10 <sup>-7</sup> (4.9x10 <sup>-8</sup> )
Nb6-bi	I	Biphasic	Biphasic	Biphasic	NP	NP	NP	NP	6.3x10 <sup>-8</sup> (1.5x10 <sup>-8</sup> )	NP
Nb6-tri	I	Biphasic	Biphasic	Biphasic	NP	NP	NP	1.5x10 <sup>-9</sup> (5.2x10 <sup>-10</sup> )	1.2x10 <sup>-9</sup> (2.5x10 <sup>-10</sup> )	1.6x10 <sup>-10</sup> (2.6x10 <sup>-11</sup> )
Nb11-tri	I	Biphasic	Biphasic	Biphasic	NP	NP	NP	NP	5.1x10 <sup>-8</sup> (1.6x10 <sup>-8</sup> )	NP
ACE2-Fc	N/A	NP	NP	NP	NP	NP	NP	5.3x10 <sup>-9</sup> (2.5x10 <sup>-9</sup> )	4.0x10 <sup>-8</sup> (8.8x10 <sup>-9</sup> )	2.6x10 <sup>-8</sup> (8.5x10 <sup>-9</sup> )
mNb6-tri	I	1.4x10 <sup>6</sup>	<1.0x10 <sup>-6</sup>	<1.0x10 <sup>-12</sup>	NP	NP	NP	4.0x10 <sup>-10</sup> (1.4x10 <sup>-10</sup> )	1.2x10 <sup>-10</sup> (2.8x10 <sup>-11</sup> )	5.4x10 <sup>-11</sup> (1.0x10 <sup>-11</sup> )

397

398 <sup>a</sup>Average values from n = 5 biological replicates for Nb6, Nb11, Nb15, Nb19 are presented, all

399 others were tested with n = 3 biological replicates.

400 <sup>b</sup>Average values from n = 2 biological replicates for Nb12, Nb17, and Nb11-tri are presented, all  
401 others were tested with n = 3 biological replicates.

402 <sup>c</sup>Average values from n = 2 biological replicates for Nb3, Nb3-bi, and Nb3-tri. n = 3 biological  
403 replicates for all others.

404 NB – no binding

405 NC – no competition

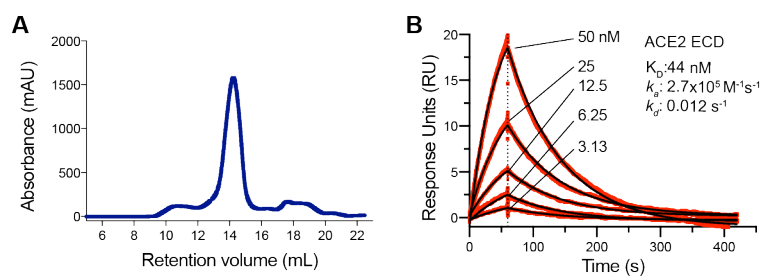
406 NP – not performed

407

408

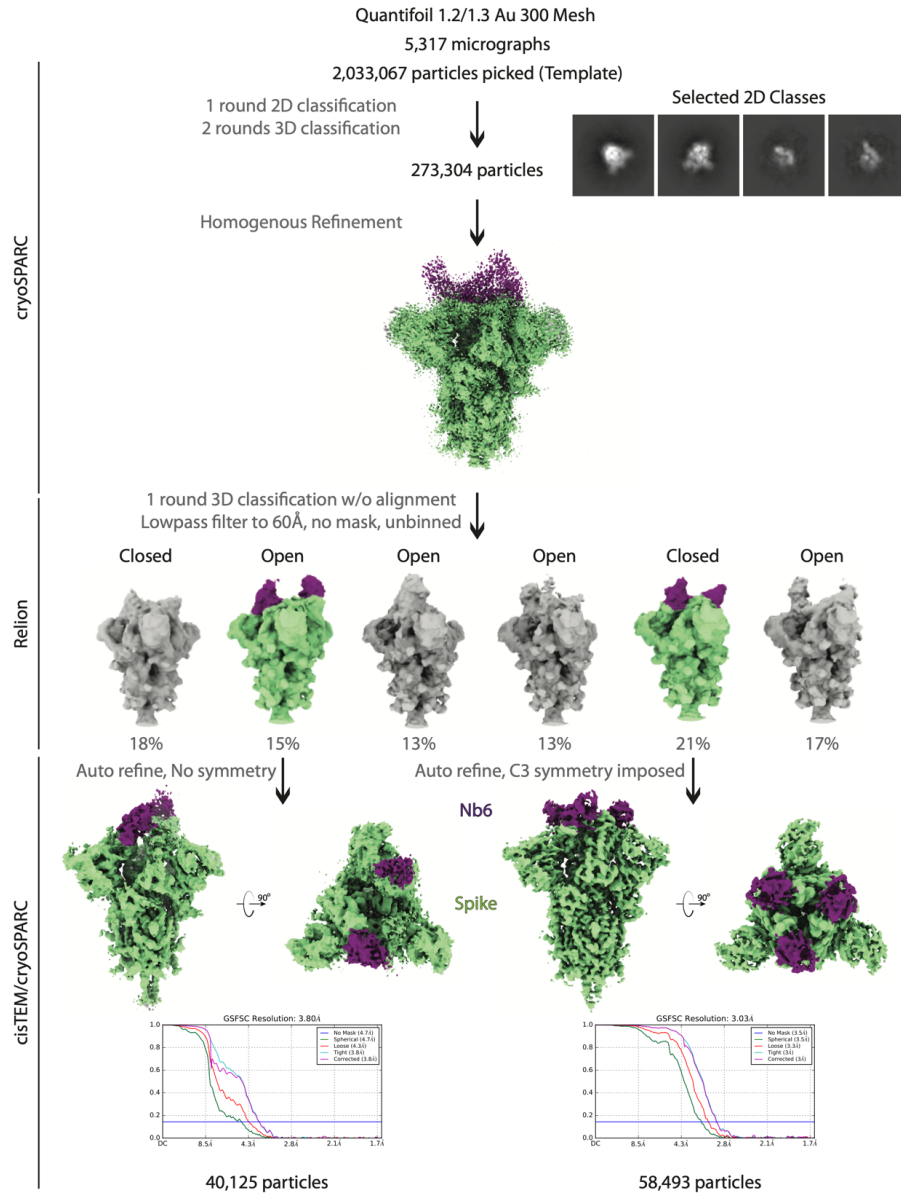
409 **Supplementary Figures**

410



411

412 **Supplementary Fig. 1. Validation of purified Spike\*.** **A**, Size exclusion chromatogram of  
413 purified Spike\* from ExpiCHO cells. **B**, SPR of immobilized Spike\* binding to monomeric ACE2  
414 extracellular domain (ECD).

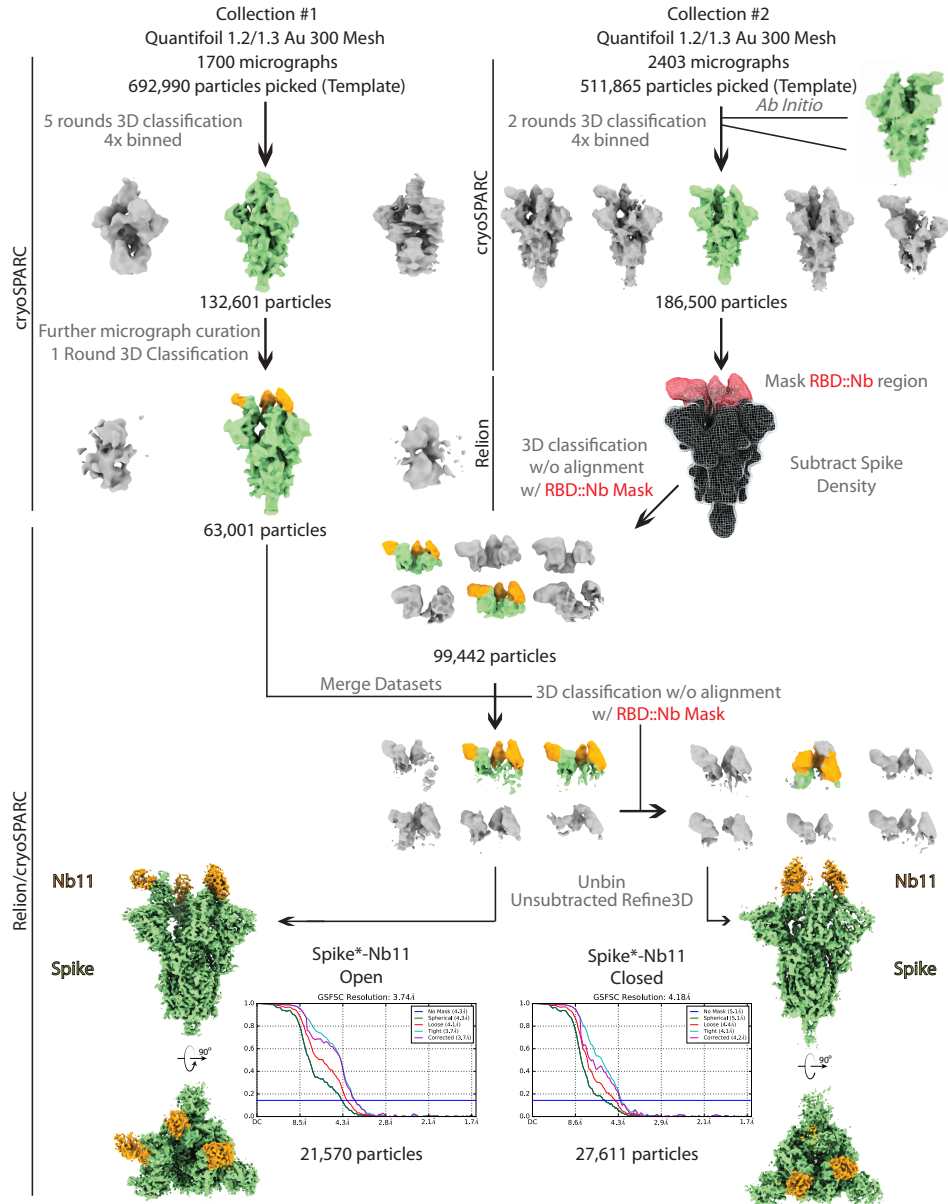


415

416 **Supplementary Fig. 2. Cryo-EM workflow for Nb6**

417 A flowchart representation of the classification workflow for Spike\*-Nb6 complexes yielding open  
 418 and closed Spike\* conformations. From top to bottom, particles were template picked with a set  
 419 of 20 Å low-pass filtered 2D backprojections of apo-Spike\* in the closed conformation. Extracted  
 420 particles in 2D classes suggestive of various Spike\* views were subject to a round of  
 421 heterogenous refinement 3 in cryoSPARC with two naïve classes generated from a truncated *Ab*  
 422 *initio* job, and a 20 Å low-pass filtered volume of apo-Spike\* in the closed conformation.  
 423 Particles in the Spike\* 3D class were subject to 25 iterations of 3D classification into 6 classes  
 424 without alignment in RELION, using the same input volume from cryoSPARC 3D classification,

425 low pass filtered to 60 Å, T = 8. Particles in classes representing the open and closed Spike\*  
426 conformations were imported into cisTEM for automatic refinement. Half maps from refinement  
427 were imported into cryoSPARC for local resolution estimation as shown in Supplementary Fig.  
428 4.



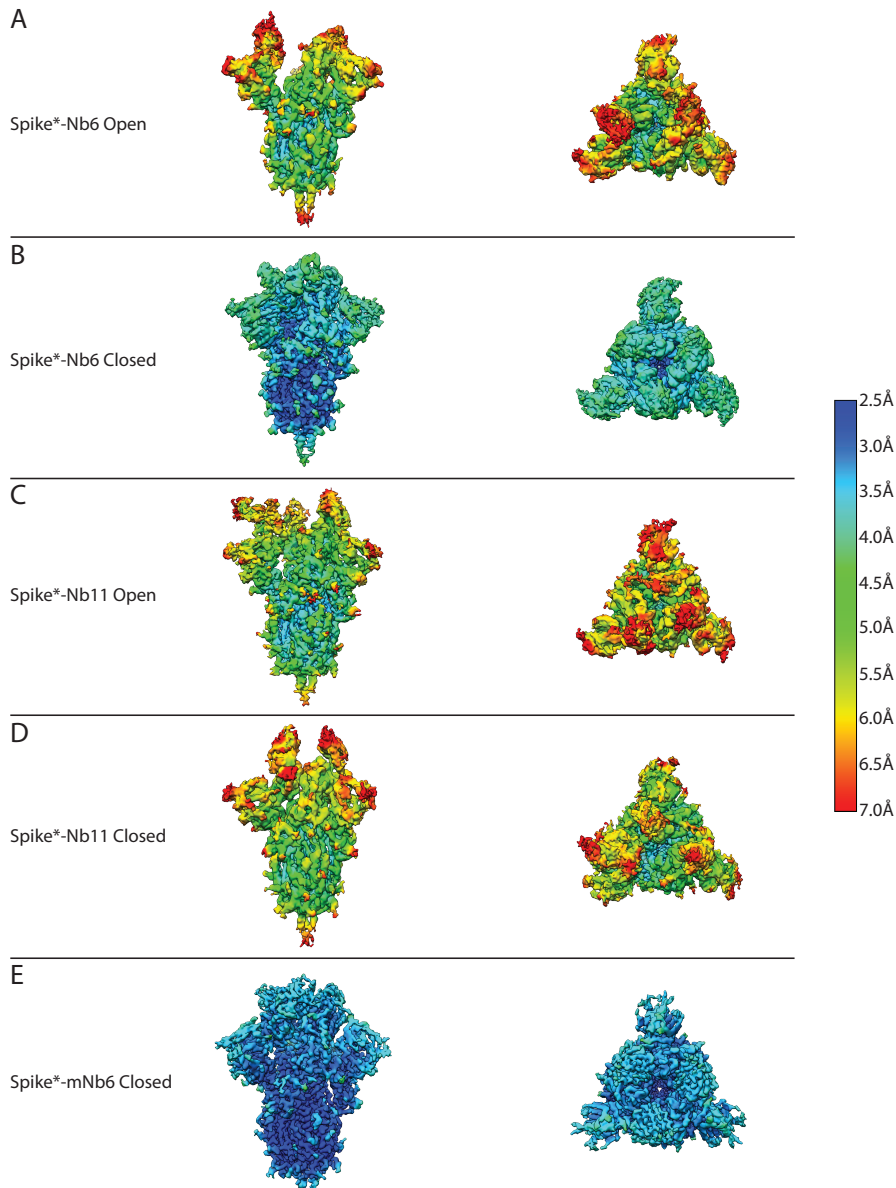
429

### 430 **Supplementary Fig. 3. Cryo-EM workflow for Nb11**

431 A flowchart representation of the classification workflow for Spike\*-Nb11 complexes yielding  
 432 open and closed Spike\* conformations. From top to bottom, particles were template picked from  
 433 two separate collections with a set of 20 Å low-pass filtered 2D backprojections of apo-Spike\* in  
 434 the closed conformation. Extracted particles were Fourier cropped to 128 pixels prior to  
 435 extensive heterogeneous refinement in cryoSPARC, using a 20 Å low-pass filtered volume of  
 436 apo-Spike\* in the closed conformation and additional naïve classes for removal of non-Spike\*  
 437 particles. After cryoSPARC micrograph curation and heterogeneous refinement, Spike\* density  
 438 corresponding to all regions outside of the ACE2 RBD::Nanobody interface were subtracted. A

439 mask around the ACE2 RBD::Nanobody interface was generated, and used for multiple rounds  
440 of 3D classification without alignment in RELION. Particles in classes representing open and  
441 closed Spike\* conformations were selected, unsubtracted and unbinned prior to refinement in  
442 RELION. Half maps from refinement were imported into cryoSPARC for local resolution  
443 estimation as shown in Supplementary Fig. 4.



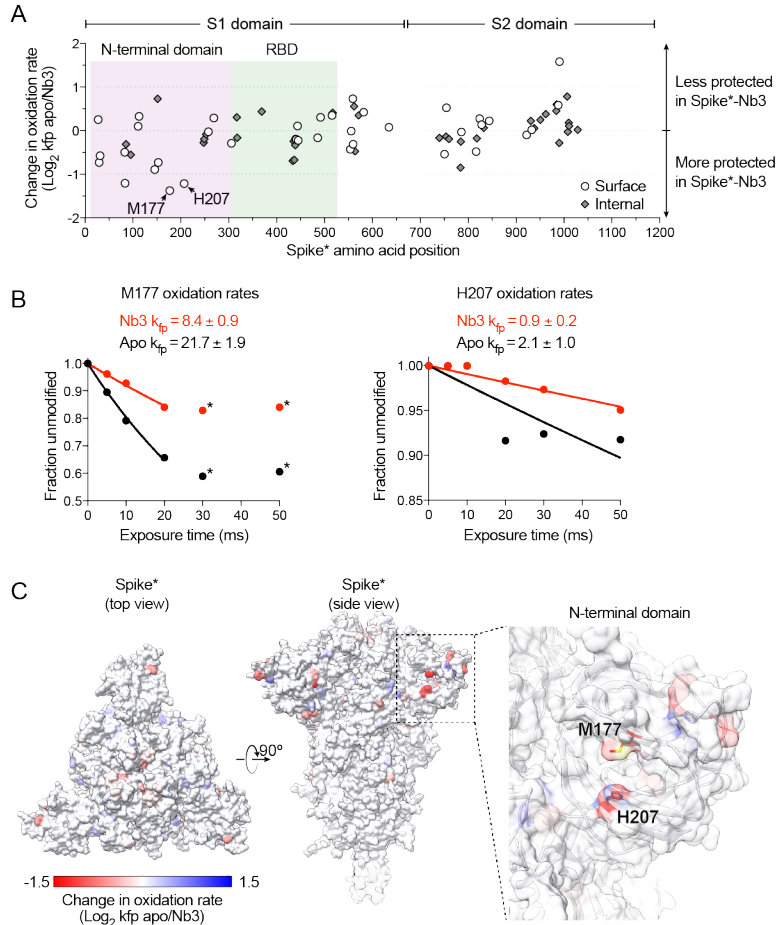


444

445 **Supplementary Fig. 4. Local resolution of cryo-EM maps**

446 Local resolution estimates of Spike\* complexes with A-B) Nb6, C-D) Nb11, and E) mNb6 as  
447 generated in cryoSPARC. All maps (except mNb6) are shown with the same enclosed volume.

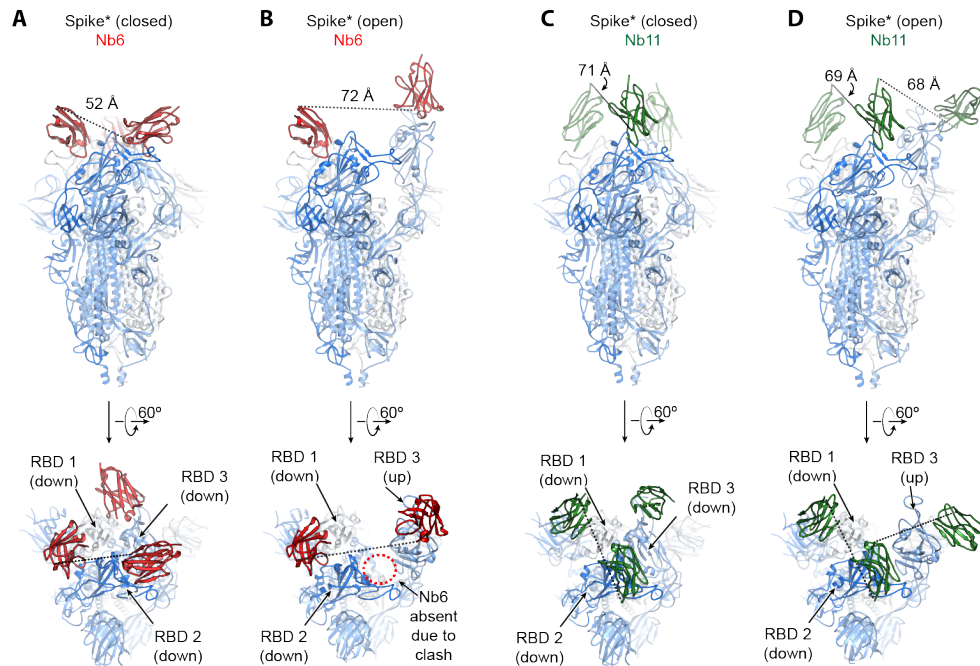
448 All maps are colored on the same scale, as indicated.



449

450 **Supplementary Fig. 5. Radiolytic hydroxyl radical footprinting of Spike\*.**

451 **A**, Change in oxidation rate between Spike\* and Nb3-Spike\* complexes at all residues. A  
452 cluster of highly protected residues in the Spike\*-Nb3 complex is observed in the N-terminal  
453 domain. **B**, Oxidation rate plots of the two (M177, H207) most heavily protected residues upon  
454 Nb3 binding to Spike\*. Data points labeled with an asterisk are excluded from rate calculations  
455 as these values fall outside of the first order reaction, likely due to extensive oxidation-mediated  
456 damage. **C**, Change in oxidation rate mapped onto Spike in the all RBD down conformation.



457

458

459 **Supplementary Fig. 6. Modeling of distances for multimeric nanobody design.** **A**, Model of

460 Spike\*:Nb6 complex in the closed state. The minimal distance between adjacent Nb6 N- and C-

461 termini is 52 Å (dashed line). **B**, Model of Spike\*:Nb6 complex in the open state with Nb6

462 docked into the cryo-EM density for up-state RBD. Minimal distance between N- and C-termini

463 of both nanobodies is 72 Å. Nb6 cannot bind RBD2 in open Spike\*, as this would sterically clash

464 with RBD3. **C**, Model of Spike\*:Nb11 complex in the closed state. The minimal distance

465 between adjacent Nb6 N- and C-termini is 71 Å (dashed line). **D**, Model of Spike\*:Nb11 complex

466 in the open state. The minimal distance between adjacent Nb6 N- and C-termini is 68 Å

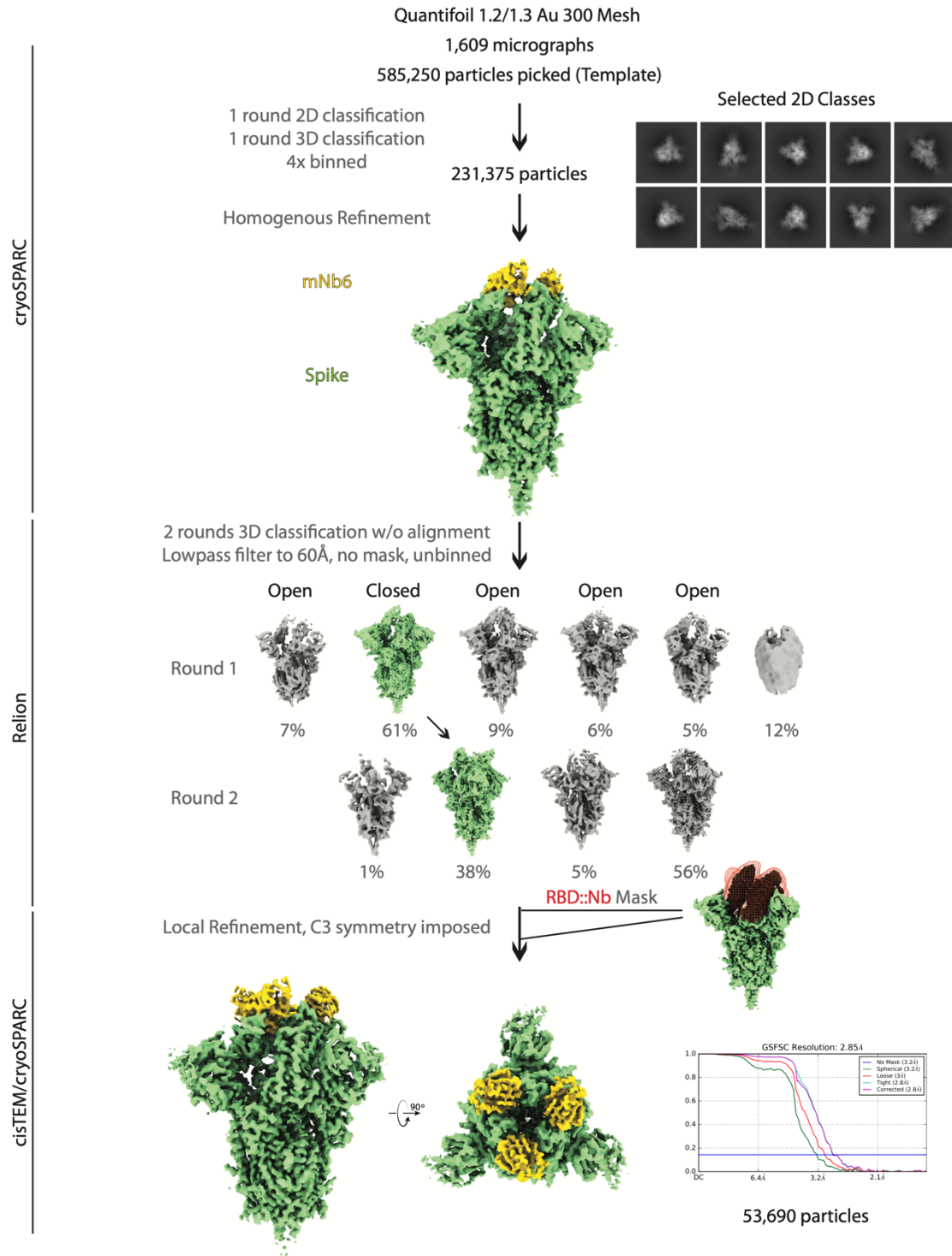
467 between Nb11 bound to RBD2 in the down-state and RBD3 in the up-state. For B, the model of

468 Nb6 from A was docked into the cryo-EM map to enable modeling of distance between N- and

469 C-termini. For C and D, a generic nanobody was docked into cryo-EM maps to model the

470 distance between N- and C-termini.

471



472

473 **Supplementary Fig. 7. CryoEM workflow for mNb6**

474 A flowchart representation of the classification workflow for the Spike\*-mNb6 complex yielding a  
 475 closed Spike\* conformation. From top to bottom, particles were template picked from two  
 476 separate collections with a set of 20Å low-pass filtered 2D backprojections of apo-Spike\* in the

477 closed conformation. Extracted particles were Fourier cropped to 96 pixels prior to 2D  
478 classification. Particles in Spike\* 2D classes were selected for a round of heterogeneous  
479 refinement in cryoSPARC using a 20 Å low-pass filtered volume of apo-Spike\* in the closed  
480 conformation and additional naïve classes for removal of non-Spike\* particles. In RELION,  
481 particles in the Spike\* 3D class were subject to two rounds of 3D classification without  
482 alignment into 6 classes using the same input volume from cryoSPARC 3D classification, low  
483 pass filtered to 60 Å, T = 8. Unbinned particles in the Spike\*-closed conformation were exported  
484 into cisTEM for automatic refinement, followed by local refinement using a mask around the  
485 ACE2 RBD::Nanobody interface. Half maps from refinement were imported into cryoSPARC for  
486 local resolution estimation as shown in Supplementary Fig. 4.

487

488

489 **Supplementary Table 1. CryoEM datasets**

Sample:	Spike*-Nb6		Spike*-Nb11		Spike*-mNb6
Spike* conformation:	Open	Closed	Open	Closed	Closed
EMDB:	XXXX	XXXX	XXXX	XXXX	XXXX
PDB:		XXXX			XXXX
<b>Data collection and processing</b>	Titan Krios/Gatan K3 with Gatan Bioquantum Energy Filter				
Microscope/Detector	SerialEM, 3x3 image shift				
Imaging software and collection					
Magnification	105,000				
Voltage (kV)	300				
Electron exposure (e-/Å <sup>2</sup> )	66				
Dose rate (e-/pix/sec)	8				
Frame exposure (e-/Å <sup>2</sup> )	0.55				
Defocus range (µm)	-0.8 to -2.0				
Pixel size (Å)	0.834 (physical)				
Micrographs	5,317		4,103		1,609
<b>Reconstruction</b>	2,033,067		1,204,855		585,250
Autopicked particles					
(template-based in cryosparc)					
Particles in final refinement	40,125	58,493	21,570	27,611	53,690
	(cisTEM)	(cisTEM)	(cisTEM)	(RELION)	(cisTEM)
Symmetry imposed	C1	C3	C1	C1	C3
Map sharpening B factor (Å <sup>2</sup> )		-90			-140
Map resolution, global FSC (Å)					
FSC 0.5, unmasked/masked	7.8/4.6	4.1/3.4	7.0/4.4	7.6/5.3	3.9/3.3
FSC 0.143, unmasked/masked	4.7/3.8	3.5/3.0	4.3/3.7	5.1/4.2	3.2/2.9
<b>Refinement</b>					
Initial model used (PDB code)	6VXX, 3P0G				6VXX, 3P0G
Model resolution (Å)					
FSC 0.5, unmasked/masked	3.5/3.1				3.2/2.9
Model composition					
Non-hydrogen atoms	26904				27015
Protein residues	3360				3360
B factors (Å <sup>2</sup> )					
Protein	97.0				57.5
Ligand	107.4				85.7
R.m.s. deviations					
Bond lengths (Å)	0.014				0.007
Bond angles (°)	1.379				1.027
Validation					
MolProbity score	1.99				1.71
Clashscore	12.70				6.46
Poor rotamers (%)	0.45				0.41
EMRinger score	2.98				4.01
CaBLAM score	3.11				2.95
Ramachandran plot					
Favored (%)	94.49				94.92
Allowed (%)	5.51				5.08
Disallowed (%)	0				0

490

491

492 **Supplementary Table 2. X-ray data collection and refinement statistics**

	mNb6 (PDB XXXX)
<b>Data collection</b>	
Space group	$P2_1$
Cell dimensions	
<i>a</i> , <i>b</i> , <i>c</i> (Å)	44.56, 71.25, 46.43
$\alpha$ , $\beta$ , $\gamma$ (°)	90.0, 114.93, 90.0
Molecules in asymmetric unit	2
Resolution (Å)	71.25 - 2.05 (2.09 - 2.05) <sup>a</sup>
$R_{\text{sym}}$ or $R_{\text{merge}}$	0.13 (0.94) <sup>b</sup>
$I / \sigma I$	7.2 (0.9)
Completeness (%)	97.8 (96.6)
Redundancy	6.4 (5.7)
CC (1/2) (%)	99.8 (64.4)
<b>Refinement</b>	
Resolution (Å)	71.25 – 2.05
No. reflections	104195
$R_{\text{work}} / R_{\text{free}}$ (%)	21.16 / 24.75
No. atoms	
Protein	1798
Ligand/ion	21
Water	131
<i>B</i> -factors	
Protein	33.1
Ligand/ion	76.1
Water	42.2
R.m.s. deviations	
Bond lengths (Å)	0.07
Bond angles (°)	0.826
Ramachandran plot	
Allowed (%)	99.06
Generous (%)	0.94
Disallowed (%)	0

493 <sup>a</sup> Values in parentheses correspond to the highest resolution shell.

494 <sup>b</sup>  $R_{\text{merge}} = \sum |I - \langle I \rangle| / \sum I$

495 <sup>c</sup>  $R_{\text{work}} = \sum |F_o - F_c| / \sum F_o$

496 <sup>d</sup>  $R_{\text{free}} = \sum |F_o - F_c| / \sum F_o$ , calculated using a random set containing 5% reflections that were not included throughout  
497 structure refinement.

498 **Supplementary Table 3. Nanobody expression plasmids**  
 499

Plasmid	Nanobody	Plasmid backbone	Resistance Marker
pPW3544	Nb2	pet-26b(+)	kanamycin
pPW3545	Nb3	pet-26b(+)	kanamycin
pPW3546	Nb6	pet-26b(+)	kanamycin
pPW3547	Nb8	pet-26b(+)	kanamycin
pPW3548	Nb11	pet-26b(+)	kanamycin
pPW3549	Nb12	pet-26b(+)	kanamycin
pPW3550	Nb15	pet-26b(+)	kanamycin
pPW3551	Nb16	pet-26b(+)	kanamycin
pPW3552	Nb17	pet-26b(+)	kanamycin
pPW3553	Nb18	pet-26b(+)	kanamycin
pPW3554	Nb19	pet-26b(+)	kanamycin
pPW3555	Nb24	pet-26b(+)	kanamycin
pPW3557	Trivalent Nb6, 20AA length GS linker	pet-26b(+)	kanamycin
pPW3558	Trivalent Nb3, 15AA length GS linker	pet-26b(+)	kanamycin
pPW3559	Trivalent Nb11, 15AA length GS linker	pet-26b(+)	kanamycin
pPW3560	Bivalent Nb3, 15AA length GS linker	pet-26b(+)	kanamycin
pPW3561	Bivalent Nb6, 15AA length GS linker	pet-26b(+)	kanamycin
pPW3563	Trivalent mNb6, 20AA length GS linker	pet-26b(+)	kanamycin
pPW3564	mNb6	pet-26b(+)	kanamycin

500  
 501  
 502



503 **METHODS**

504 **Expression and purification of SARS-CoV-2 Spike, RBD, and ACE2.**

505 We used a previously described construct to express and purify the pre-fusion SARS-CoV-2  
506 Spike ectodomain (Spike\*) [15]. ExpiCHO or Expi293T cells (ThermoFisher) were transfected  
507 with the Spike\* construct per the manufacturer's instructions for the MaxTiter protocol and  
508 harvested between 3-9 days after transfection. Clarified cell culture supernatant was loaded  
509 onto Ni-Excel beads (Cytiva) followed by extensive washes in 20 mM HEPES pH 8.0, 200 mM  
510 sodium chloride, and 10 mM imidazole and elution in the same buffer supplemented with 500  
511 mM imidazole. Spike\* was concentrated using a 100 kDa MWCO spin concentrator (Millipore)  
512 and further purified by size exclusion chromatography over a Superose 6 Increase 10/300  
513 column (GE Healthcare) in 20 mM HEPES pH 8.0 and 200 mM sodium chloride. All purification  
514 steps were performed at room temperature. The resulting fractions for trimeric Spike\* were  
515 pooled and either used directly for cryo-EM studies or concentrated and flash frozen in liquid  
516 nitrogen with 15% glycerol for other biochemical studies.

517  
518 We used a previously described construct to express and purify the SARS-CoV-2 Receptor  
519 binding domain (RBD) [43]. Expi293T cells (ThermoFisher) were transfected with the RBD  
520 construct per the manufacturer's instructions and harvested between 3-6 days after transfection.  
521 Clarified cell culture supernatant was loaded onto Ni-Excel beads (Cytiva) or a His-Trap Excel  
522 column (GE Healthcare) followed by washes in 20 mM HEPES pH 8.0, 200 mM sodium  
523 chloride, and 10 mM imidazole and elution using the same buffer supplemented with 500 mM  
524 imidazole. RBD was concentrated using a 30 kDa MWCO spin concentrator (Millipore) and  
525 further purified by size exclusion chromatography over a Superdex 200 Increase 10/300 GL  
526 column (GE Healthcare) in 20 mM HEPES pH 8.0 and 200 mM sodium chloride. The resulting  
527 fractions were pooled, concentrated, and flash frozen in liquid nitrogen with 10% glycerol.

528  
529 For biochemical and yeast display experiments, Spike\* and RBD were labeled with freshly  
530 prepared stocks of Alexa 647-NHS, Alexa 488-NHS, or Biotin-NHS (ThermoFisher) with a 5-fold  
531 stoichiometry for 1 hour at room temperature followed by quenching of NHS with 10 mM Tris pH  
532 8.0 for 60 minutes. Labeled proteins were further purified by size exclusion chromatography,  
533 concentrated using a spin concentrator (Millipore), and flash frozen in liquid nitrogen with 10-  
534 15% glycerol.

535

536 We used an ACE2-ECD (18-614) Fc fusion expression plasmid to express and purify Fc tagged  
537 ACE2-ECD [44]. Expi293T cells (ThermoFisher) were transfected with the ACE2-Fc construct  
538 per the manufacturer's instructions and harvested between 5-7 days after transfection. Clarified  
539 cell culture supernatant was loaded onto a MabSelect Pure 1 mL Column (GE Healthcare).  
540 Column was washed with Buffer A (20 mM HEPES pH 7.5, 150 mM NaCl) and protein was  
541 eluted with Buffer B (100 mM Sodium Citrate pH 3.0, 150 mM NaCl) into a deep well block  
542 containing 1 M HEPES pH 7.5 to neutralize the acidic elution. ACE2-Fc was concentrated using  
543 a 30 kDa MWCO spin concentrator (Millipore) and further purified by size exclusion  
544 chromatography over a Superdex 200 Increase 10/300 GL column (GE Healthcare) in SEC  
545 Buffer (20 mM HEPES pH 7.5, 150 mM NaCl, 5% v/v Glycerol). The resulting fractions were  
546 pooled, concentrated, and flash frozen in liquid nitrogen. To obtain monomeric ACE2, 1:50  
547 (w/w) His-tagged TEV protease was added to ACE2-Fc and incubated at 4 °C overnight. This  
548 mixture was then purified by size exclusion chromatography in SEC Buffer. Monomeric ACE2  
549 fractions were pooled and washed with His-resin (1 mL of 50% slurry) to remove excess TEV.  
550 The resulting supernatant was pooled, concentrated, and flash frozen in liquid nitrogen.

551

#### 552 **Identification of anti SARS-CoV2 Spike nanobodies**

553 To identify nanobodies against the SARS-CoV-2 Spike ECD, we used a yeast surface displayed  
554 library of synthetic nanobody sequences that recapitulate amino acid position specific-variation  
555 in natural llama immunological repertoires. This library encodes a diversity of  $>2 \times 10^9$  variants,  
556 and uses a synthetic stalk sequence for nanobody display, as described previously in a modified  
557 vector encoding nourseothricin (NTC) resistance [45]. For the first round of selection,  $2 \times 10^{10}$   
558 yeast induced in YPG (Yeast Extract-Peptone-Galactose) supplemented with NTC were washed  
559 repeatedly in selection buffer (20 mM HEPES, pH 7.5, 150 mM sodium chloride, 0.1% (w/v) low  
560 biotin bovine serum albumin, BSA) and finally resuspended in 10 mL of selection buffer  
561 containing 200 nM biotinylated-Spike\*. Yeast were incubated for 30 minutes at 25 °C, then  
562 washed repeatedly in cold selection buffer, and finally resuspended in 10 mL of cold selection  
563 buffer containing 200  $\mu$ L of Miltenyi anti-Streptavidin microbeads. After 30 minutes of incubation  
564 at 4 °C, yeast were again washed with cold selection buffer. Spike\* binding yeast were captured  
565 on a Miltenyi MACS LS column and recovered in YPD (Yeast Extract-Peptone-Dextrose)  
566 medium supplemented with NTC.

567

568 For round 2,  $4 \times 10^8$  induced yeast from Round 1 were incubated with 100 nM Spike\* labeled with  
569 Alexa647 in 1 mL of selection buffer for 1 hr at 25 °C. After extensive washes with cold selection

570 buffer, Spike\* binding yeast were isolated by fluorescence activated cell sorting (FACS) on a  
571 Sony SH800 instrument. A similar approach was used for round 3, with substitution of 10 nM  
572 Spike\* labeled with Alexa647. Post round 3 yeast were plated on YPD+NTC solid media and  
573 768 individual colonies were induced with YPG+NTC media in 2 mL deep well plates. Each  
574 individual clone was tested for binding to 4 nM Spike\*-Alexa488 by flow cytometry on a  
575 Beckman Coulter Cytotflex. To identify nanobodies that disrupt Spike-ACE2 interactions, Spike\*  
576 binding was repeated in the presence of 0.5-1  $\mu$ M ACE2-Fc. Out of 768 clones, we identified 21  
577 that strongly bind Spike\* and are competitive with ACE2 (Supplementary Table 3).

578

### 579 **Expression and purification of nanobodies**

580 Nanobody sequences were cloned into the pET26-b(+) expression vector using In-Fusion HD  
581 cloning (Takara Bio), transformed into BL21(DE3) *E. coli*, grown in Terrific Broth at 37 °C until  
582 OD 0.7-0.8, followed by gene induction using 1 mM IPTG for 18-22 hours at 25°C. *E. Coli* were  
583 harvested and resuspended in SET Buffer (200 mM Tris, pH 8.0, 500 mM sucrose, 0.5 mM  
584 EDTA, 1X cOmplete protease inhibitor (Roche)) for 30 minutes at 25 °C before a 45 minute  
585 osmotic shock with a two-fold volume addition of water. NaCl, MgCl<sub>2</sub>, and imidazole were  
586 added to the lysate to 150 mM, 2 mM, and 40 mM respectively before centrifugation at 17-  
587 20,000xg for 15 minutes to separate cell debris from the periplasmic fraction. For every liter of  
588 bacterial culture, the periplasmic fraction was then incubated with 4 mL of 50% HisPur Ni-NTA  
589 resin (Thermo Scientific) which had been equilibrated in Nickel Wash Buffer (20 mM HEPES,  
590 pH 7.5, 150 mM NaCl, 40 mM imidazole). This mixture was incubated for 1 hr with rotation at  
591 RT before centrifugation at 50xg to collect the resin. The resin was then washed with 5 volumes  
592 of Nickel Wash buffer 3 times, each time using centrifugation to remove excess wash buffer.  
593 Bound proteins were then eluted using three washes with Elution Buffer (20 mM HEPES, pH  
594 7.5, 150 mM NaCl, 500 mM imidazole). The eluted protein was concentrated using a 3.5 kDa  
595 MWCO centrifugal filter unit (Amicon) before injection onto a Superdex 200 Increase 10/300 GL  
596 column equilibrated with 20 mM HEPES, pH 7.5, 150 mM NaCl. Nanobody constructs were  
597 concentrated again using a 3.5k MWCO centrifugal filter unit, and flash frozen in liquid nitrogen.

598

### 599 **Affinity determination by surface plasmon resonance**

600 Nanobody (Nb) affinity determination experiments were performed on Biacore T200 and 8K  
601 instruments (Cytiva Life Sciences) by capturing the StreptagII-tagged Spike\* at 10  $\mu$ g/mL on a  
602 StreptactinXT-immobilized (Iba Life Sciences) CM5 Series S sensor chip (Cytiva Life Sciences)  
603 to achieve maximum response (R<sub>max</sub>) of approximately 30 response units (RUs) upon

604 nanobody binding. 2-fold serial dilutions of purified nanobody from 1  $\mu$ M to 31.25 nM (for  
605 monovalent constructs) or from 50 nM to 1.56 nM (for affinity matured and multimeric  
606 constructs) were flowed over the captured Spike\* surface at 30  $\mu$ L/minute for 60 seconds  
607 followed by 600 seconds of dissociation flow. Following each cycle, the chip surface was  
608 regenerated with 3 M guanidine hydrochloride.

609  
610 Separately, biotinylated SARS-CoV-2 RBD at 8  $\mu$ g/mL was loaded onto a preconditioned Series  
611 S Sensor Chip CAP chip (Cytiva Life Sciences) to achieve an R<sub>max</sub> of approximately 60 RUs  
612 upon nanobody binding. 2-fold serial dilutions in the same running buffer and sample series  
613 (parent or affinity matured clone) as the Spike\* runs were flowed over the RBD surface at 30  
614  $\mu$ L/minute for 60 seconds followed by 600 seconds of dissociation flow. Chip surface  
615 regeneration was performed with a guanidine hydrochloride/sodium hydroxide solution.

616  
617 The resulting sensorgrams for all monovalent clones were fit to a 1:1 Langmuir binding model  
618 using the Biacore Insight Evaluation Software (Cytiva Life Sciences) or the  
619 association/dissociation model in GraphPad Prism 8.0. For determination of kinetic parameters  
620 for Nb6-bi and Nb6-tri binding, the dissociation phase was fit to a biexponential decay  
621 constrained to two dissociation rate constants shared between each concentration. The  
622 association phase was fit separately using an association kinetics model simultaneously fitting  
623 the association rate constant for each concentration.

624  
625 For nanobody competition experiments, Spike\* was loaded onto a StreptactinXT-immobilized  
626 CM5 sensor chip as previously described. As in the kinetics experiments, the primary nanobody  
627 was flowed over the captured Spike\* surface for 60 seconds at 30  $\mu$ L/minute to achieve  
628 saturation. Immediately following this, a second injection of a mixture of primary and variable  
629 nanobody at the same concentration as in the primary injection was performed.

630

### 631 **ACE2 cellular surface binding competition assays**

632 A dilution series of nanobody was generated in PBE (PBS + 0.5% (w/v) BSA + 2 mM EDTA and  
633 mixed with Spike\*-Alexa647 or RBD-Alexa647. ACE2 expressing HEK293T cells were  
634 dissociated with TrypLE Express (ThermoFisher) and resuspended in PBE [20]. The cells were  
635 mixed with the Spike\*-nanobody solution and incubated for 45 minutes, washed in PBE, and  
636 then resuspended in PBE. Cell surface Alexa647 fluorescence intensity was assessed on an  
637 Attune Flow Cytometer (ThermoFisher).

638

### 639 **Affinity maturation of Nb6**

640 A site saturation mutagenesis library of Nb6 was generated by assembly PCR of overlapping  
641 oligonucleotides encoding the Nb6 sequence. Individual oligos for each position in CDR1,  
642 CDR2, and CDR3 were designed with the degenerate “NNK” codon. The assembled gene  
643 product was amplified with oligonucleotides with overlapping ends to enable homologous  
644 recombination with the yeast surface display vector as previously described and purified with  
645 standard silica-based chromatography [45]. The resulting insert DNA was transformed into  
646 *Saccharomyces cerevisiae* strain BJ5465 along with the yeast display vector pYDS2.0 to  
647 generate a library of  $2 \times 10^8$  transformants. After induction in YPD+NTC medium at 20 °C for 2  
648 days,  $2 \times 10^9$  yeast were washed in selection buffer (20 mM HEPES, pH 8.0, 150 mM sodium  
649 chloride, 0.1% (w/v) low biotin BSA) and incubated with 1 nM biotin-Spike\* for 1 hour at 25 °C.  
650 Yeast were subsequently washed in selection buffer, resuspended in 1 mL selection buffer, and  
651 incubated with 10  $\mu$ L streptavidin microbeads (Miltenyi) for 15 min. at 4 °C. Yeast were washed  
652 again with cold selection buffer and Spike\*-binding yeast were isolated by magnetic separation  
653 using an LS column (Miltenyi). Recovered yeast were grown in YPD+NTC at 37 °C and induced  
654 in YPG+NTC at 20 °C. A second round of selection was performed as above, substituting 100  
655 pM RBD-Alexa647 as the antigen. Yeast displaying high affinity clones were selected by  
656 magnetic separation using Anti-Cy5 microbeads (Miltenyi) and an LS column. Analysis of the  
657 library after the second round of selection revealed a population of clones with clear binding of  
658 10 pM RBD-Alexa647. Therefore, 96 individual clones were screened for binding to 10 pM RBD-  
659 Alexa647 by flow cytometry. Sequence analysis of eight clones that showed robust binding to  
660 10 pM RBD-Alexa647 revealed two consensus mutations, I27Y and P105Y, which were used to  
661 generate the affinity matured clone mNb6.

662

### 663 **Structures of Spike-nanobody complexes by cryo-EM**

#### 664 *Sample preparation and microscopy*

665 To prepare Spike\*-nanobody complexes, each nanobody was incubated on ice at a 3-fold molar  
666 excess to Spike\* at 2.5  $\mu$ M for 10 minutes. 3  $\mu$ L of Spike\*-nanobody complex was added to a  
667 300 mesh 1.2/1.3R Au Quantifoil grid previously glow discharged at 15 mA for 30 seconds.  
668 Blotting was performed with a blot force of 0 for 4 seconds at 4 °C and 100% humidity in a FEI  
669 Vitrobot Mark IV (ThermoFisher) prior to plunge freezing into liquid ethane.

670

671 For each complex, 120-frame super-resolution movies were collected with a 3x3 image shift  
672 collection strategy at a nominal magnification of 105,000x (physical pixel size: 0.834 Å/pix) on a  
673 Titan Krios (ThermoFisher) equipped with a K3 camera and a Bioquantum energy filter (Gatan)  
674 set to a slit width of 20 eV. Collection dose rate was 8 e<sup>-</sup>/pixel/second for a total dose of 66 e<sup>-</sup>  
675 /Å<sup>2</sup>. Each collection was performed with semi-automated scripts in SerialEM [46].

676

### 677 *Image Processing*

678 For all datasets, dose fractionated super-resolution movies were motion corrected with  
679 MotionCor2 [47]. Contrast transfer function determination was performed with cryoSPARC patch  
680 CTF [48]. Particles were picked with a 20 Å low-pass filtered apo Spike 2D templates generated  
681 from a prior data collection.

682

683 Nb6-Spike\* and mNb6-Spike\* particles were extracted with a 384 pixel box, binned to 96 pixels  
684 and subject to single rounds of 2D and 3D classification prior to unbinning for homogenous  
685 refinement in cryoSPARC [48]. Refined particles were then imported into Relion3.1 for 3D  
686 classification without alignment using the input refinement map low pass filtered to 40 Å [49].  
687 Particles in classes representing the closed conformation of Spike were imported into cisTEM  
688 and subject to autorefinement followed by local refinement within a RBD::nanobody masked  
689 region [50]. Following local refinement, a new refinement package symmetrized to the C3 axis  
690 was created for a final round of local refinement without masking. Final particle counts for each  
691 map are as follows: Nb6-Open: 40,125, Nb6-Closed: 58,493, mNb6: 53,690.

692

693 Nb11-Spike\* particles were extracted with a 512 pixel box, binned to 128 pixels for multiple  
694 rounds of 3D classification as described in Figure S4. Following homogenous refinement,  
695 particles were exported to Relion3.1. Particle density roughly corresponding to RBD-nanobody  
696 complexes was retained post-particle subtraction. 3D classification without alignment was  
697 performed on the particle subtracted stacks. Particles in classes with robust RBD-nanobody  
698 density were selected, unsubtracted and refined in Relion followed by post-processing. 21,570  
699 particles contributed to the final maps. Final particle counts for each map are as follows: Nb11-  
700 Open: 21,570, Nb11-Closed: 27,611. For all maps, final local resolution estimation and GSFSC  
701 determination was carried out in cryoSPARC.

702

### 703 *Structure modeling*

704 Models of Nb6-Spike\* and mNb6-Spike\* were built using a previously determined structure of  
705 closed Spike\* (PDB: 6VXX) [14]. A composite model incorporating resolved regions of the RBD  
706 was made using a previously determined X-ray crystal structure of the SARS-CoV-2 RBD (PDB:  
707 6M0J) [51]. For Nb6, the beta2-adrenergic receptor nanobody Nb80 (PDB: 3P0G) was used as  
708 a template to first fit the nanobody into the cryo-EM density map for the Nb6-Spike\* complex  
709 [52]. Complementarity determining loops were then truncated and rebuilt using RosettaES [53].  
710 The final structure was inspected and manually adjusted in COOT and ISOLDE, followed by real  
711 space refinement in PHENIX [54-56]. The higher resolution structure of mNb6 enabled manual  
712 building of nanobody CDR loops *de novo*, and therefore the Rosetta-based approach was not  
713 used for modeling. Final models were analyzed in PHENIX, with statistics reported in  
714 Supplementary Table 1.

715

716 For models of Nb11-Spike\* complexes presented here, the closest nanobody by sequence in  
717 the PDB (beta2-adrenergic receptor Nb60, PDB ID: 5JQH) was fit by rigid-body refinement in  
718 COOT into the cryo-EM density map using only the framework regions [57]. While the lower  
719 resolution of these maps precluded confident assignment of loop conformations, the overall  
720 orientation of Nb11 relative to Spike\* was well constrained, enabling accurate modeling of  
721 distances between the N- and C- termini of two Nb11 molecules bound to Spike\*.

722

### 723 **Radiolytic hydroxyl radical footprinting and mass-spectrometry of Spike\* and Nb3-Spike\***

724 Spike\* and Nb3 samples were buffer exchanged into 10 mM phosphate buffer (pH 7.4) by  
725 extensive dialysis at 25 °C. A 1.5-fold molar excess of Nb3 was added to 5 µM Spike\* and the  
726 complex was incubated for >24 hr at 25 °C. For radiolytic footprinting, protein concentrations  
727 and beam parameters were optimized using an Alexa-488 fluorophore assay [58]. Apo Spike\*  
728 and Spike\*-Nb3 complex at concentrations of 1-3 µM were exposed to a synchrotron X-ray  
729 white beam at 6 timepoints between 0-50 ms at beamline 3.2.1 at the Advanced Light Source in  
730 Berkeley, CA and were quenched with 10 mM methionine amide immediately post-exposure.  
731 Glycans were removed by treatment with 5% SDS, 5 mM DTT at 95 °C for five minutes and  
732 subsequent PNGase (Promega) digestion at 37°C for 2 hours. Samples were buffer exchanged  
733 into ammonium bicarbonate (ABC) buffer (pH 8.0) using ZebaSpin columns (Thermo Fisher).  
734 Alkylation of cysteines was achieved by treatment with 8 M urea and 5 mM DTT at 37°C for 30  
735 minutes followed by an incubation with 15 mM iodoacetamide at 25 °C in the dark for 30  
736 minutes. All samples were further buffer exchanged to ABC pH 8.0 using ZebaSpin columns

737 and digested with either Trypsin/Lys-C or Glu-C (Promega) at an enzyme:protein ratio of 1:20  
738 (w/w) at 37 °C for 8 hours.

739

740 Samples were lyophilized and resuspended in 1% formic acid at 200 fmol/μL concentration. For  
741 each MS analysis, 1 μL of sample was injected onto a 5 mm Thermo Trap C18 cartridge, and  
742 then separated over a 15 cm column packed with 1.9 μm Reprosil C18 particles (Dr. Maisch  
743 HPLC GmbH) by a nanoElute HPLC (Bruker). Separation was performed at 50 °C and a flow  
744 rate of 400 μL/min by the following gradient in 0.1% formic acid: 2% to 17% acetonitrile from 0  
745 to 20 min, followed by 17% to 28% acetonitrile from 20 to 40 min. The eluent was electrospray  
746 ionized into a Bruker timsTOF Pro mass spectrometer and data was collected using data-  
747 dependent PASEF acquisition. Database searching and extraction of MS1 peptide abundances  
748 was performed using the FragPipe platform with either trypsin or GluC enzyme specificity, and  
749 all peptide and protein identifications were filtered to a 1% false-discovery rate [59]. Searches  
750 were performed against a concatenated protein database of the Spike protein, common  
751 contaminant proteins, and the *Saccharomyces cerevisiae* proteome (downloaded July 23,  
752 2020). Note, the *Saccharomyces cerevisiae* proteome was included to generate a sufficient  
753 population of true negative identifications for robust false discovery rate estimation of peptide  
754 and protein identifications. Lastly, the area under the curve MS1 intensities reported from  
755 FragPipe were summarized for each peptide species using MSstats [60].

756

757 The peak areas of extracted ion chromatograms and associated side-chain modifications were  
758 used to quantify modification at each timepoint. Increasing beamline exposure time decreases  
759 the fraction of unmodified peptide and can be represented as a site-specific dose-response plot  
760 (Supplementary Fig. 5B). The rate of hydroxyl radical reactivity ( $k_{fp}$ ) is dependent on both the  
761 intrinsic reactivity of each residue and its solvent accessibility and was calculated by fitting the  
762 dose-response to a pseudo-first order reaction scheme in Graphpad Prism Version 8. The ratio  
763 of  $k_{fp}$  between apo Spike\* and the Spike-Nb3 complex at specific residues gave information on  
764 solvent accessibility changes between the two samples. These changes were mapped onto the  
765 SARS-CoV-2 Spike (PDB 6XR8) [11]. In some cases, heavily modified residues show a  
766 flattening of dose-response at long exposures which we interpret as radical induced damage.  
767 These over-exposed timepoints were excluded from the calculation of  $k_{fp}$ .

768

769 **mNb6 crystallography and structure determination**



770 Purified mNb6 was concentrated to 18.7 mg/mL and filtered using 0.1  $\mu$ m hydrophilic PVDF  
771 filters (Millipore). mNb6 crystal screens were set up in 96 well plates in hanging drop format at  
772 2:1 protein:reservoir in Index and AmSO4 screens (Hampton Research, Aliso Viejo, CA).  
773 Crystals in over 60 different screening conditions with various morphologies appeared overnight  
774 at ambient temperature and were obtained directly from the screens without further optimization.  
775 The crystals were cryoprotected by quick dipping in a solution containing 80% reservoir and  
776 20% PEG400 or 20% Glycerol, then mounted in CrystalCap HT Cryoloops (Hampton Research,  
777 Aliso Viejo, CA) and flash cooled in a cryogenic nitrogen stream (100 K). All data were collected  
778 at the Advanced Light Source (Berkeley, CA) beam line 8.3.1. A single crystal of mNb6 that  
779 grew in 0.1 M Tris.HCl pH 8.5, 1.0 M Ammonium sulfate diffracted to 2.05 Å. Integration, and  
780 scaling were performed with Xia2, using XDS for indexing and integration and XSCALE for  
781 scaling and merging [61]. The structure was solved molecular replacement using PHASER  
782 using the structure of nanobody, Nb.b201 (PDB 5VNV) as search model [45, 62]. Model building  
783 was performed with COOT and refined with PHENIX and BUSTER[54, 56, 63].

784

#### 785 **Pseudovirus assays for nanobody neutralization**

786 ZsGreen SARS-CoV-2-pseudotyped lentivirus was generated according to a published protocol  
787 [20]. The day before transduction, 50,000 ACE2 expressing HEK293T cells were plated in each  
788 well of a 24-well plate. 10-fold serial dilutions of nanobody were generated in complete medium  
789 (DMEM + 10% FBS + PSG) and pseudotyped virus was added to a final volume of 200  $\mu$ L.  
790 Media was replaced with nanobody/pseudotyped virus mixture for four hours, then removed.  
791 Cells were washed with complete medium and then incubated in complete medium at 37 °C.  
792 Three days post-transduction, cells were trypsinized and the proportion of ZsGreen+ cells was  
793 measured on an Attune flow cytometer (ThermoFisher).

794

#### 795 **Authentic SARS-CoV-2 neutralization assay**

796 SARS-CoV-2, isolate France/IDF0372/2020, was supplied by the National Reference Centre for  
797 Respiratory Viruses hosted by Institut Pasteur (Paris, France) and headed by Pr. Sylvie van der  
798 Werf. Viral stocks were prepared by propagation in Vero E6 cells in Dulbecco's modified Eagle's  
799 medium (DMEM) supplemented with 2% (v/v) fetal bovine serum (FBS, Invitrogen). Viral titers  
800 were determined by plaque assay. All plaque assays involving live SARS-CoV-2 were  
801 performed at Institut Pasteur Paris (IPP) in compliance with IPP's guidelines following Biosafety  
802 Level 3 (BSL-3) containment procedures in approved laboratories. All experiments were  
803 performed in at least three biologically independent samples.

804

805 Neutralization of infectious SARS-CoV-2 was performed using a plaque reduction neutralization  
806 test in Vero E6 cells (CRL-1586, ATCC). Briefly, nanobodies (or ACE2-Fc) were eight-fold  
807 serially diluted in DMEM containing 2% (v/v) FBS and mixed with 50 plaque forming units (PFU)  
808 of SARS-CoV-2 for one hour at 37°C, 5% CO<sub>2</sub>. The mixture was then used to inoculate Vero E6  
809 cells seeded in 12-well plates, for one hour at 37 °C, 5% CO<sub>2</sub>. Following this virus adsorption  
810 time, a solid agarose overlay (DMEM, 10% (v/v) FBS and 0.8% agarose) was added. The cells  
811 were incubated for a further 3 days prior to fixation using 4% formalin and plaques visualized by  
812 the addition of crystal violet. The number of plaques in quadruplicate wells for each dilution was  
813 used to determine the half maximal inhibitory concentrations (IC<sub>50</sub>) using 3-parameter logistic  
814 regression (GraphPad Prism version 8).

815

### 816 **Nanobody stability studies**

817 Nanobody thermostability by circular dichroism was assessed using a Jasco J710 CD  
818 spectrometer equipped with a Peltier temperature control. Individual nanobody constructs were  
819 diluted to 5 µM in phosphate buffered saline. Molar ellipticity was measured at 204 nm (2 nm  
820 bandwidth) between 25 °C and 80 °C with a 1 °C/min heating rate. The resulting molar ellipticity  
821 values were normalized and plotted in GraphPad Prism 8.0 after applying a nearest neighbor  
822 smoothing function.

823

824 For nanobody competition experiments on ACE2 expressing HEK293T cells, nanobodies were  
825 incubated at either 25°C or 50°C for one hour. Alternatively, each nanobody was aerosolized  
826 with a portable mesh nebulizer producing 2-5 µm particles at a final concentration of 0.5 mg/mL.  
827 The resulting aerosol was collected by condensation into a 50 mL tube cooled on ice. Samples  
828 were then treated as indicated above to determine IC<sub>50</sub> values for binding to Spike\*-Alexa647.

829

830 Further experiments assessing mNb6 and mNb6-tri stability to aerosolization and lyophilization  
831 used a starting concentration of 0.5 mg/mL of each construct. Aerosolization was performed as  
832 described above. For lyophilization, nanobodies were first flash frozen in liquid nitrogen and the  
833 solution was dried to completion under vacuum. The resulting dried material was resuspended  
834 in 20 mM HEPES pH 7.5, 150 mM NaCl. Size exclusion chromatography of the unstressed,  
835 post-aerosolization, and post-lyophilization samples were performed on a Superdex 75 Increase  
836 10/300 column in 20 mM HEPES pH 7.5, 150 mM NaCl. SPR experiments to assess binding to  
837 Spike\* were performed as described above.

838

## 839 **Acknowledgements**

840 This work was supported by the UCSF Program for Breakthrough Biomedical Research  
841 (PBBR), which is partially funded by the Sandler Foundation. Further support was provided by  
842 the National Institutes of Health (NIH) grant DP5OD023048 (A.Manglik). Cryo-EM equipment at  
843 UCSF is partially supported by NIH grants S10OD020054 and S10OD021741. Work by  
844 M.Vignuzzi was funded by the Laboratoire d'Excellence grant ANR-10-LABX-62-IBEID and the  
845 URGENCE COVID-19 Institut Pasteur fundraising campaign. The radiolytic hydroxyl radical  
846 footprinting is supported by NIH 1R01GM126218. The Advanced Light Source is supported by  
847 the Office of Science, Office of Biological and Environmental Research, of the U.S. DOE under  
848 contract DE-AC02-05CH11231. S.Sangwan was supported by a Helen Hay Whitney  
849 postdoctoral fellowship. C.Billesbølle acknowledges support from the Alfred Benzon Foundation.  
850 K.Leon was funded by NIH/NINDS award F31NS113432 and a UCSF Discovery Fellowship  
851 from the Otellini Family. M.Ott acknowledges support through a gift from the Roddenbury  
852 Foundation. P.Walter is an Investigator of the Howard Hughes Medical Institute. A.Manglik  
853 acknowledges support from the Pew Charitable Trusts, the Esther and A. & Joseph Klingenstein  
854 Fund and the Searle Scholars Program.

855

856 We thank the entire Walter and Manglik labs for facilitating the development and rapid execution  
857 of this large-scale collaborative effort. We thank Sebastian Bernales and Tony De Fougères  
858 for advice and helpful discussion, and Jonathan Weissman for input into the project and reagent  
859 and machine use. We thank Jim Wells for providing the ACE2 ECD-Fc construct, Jason  
860 McLellan for providing Spike, RBD, and ACE2 constructs, and Florian Krammer for providing an  
861 RBD construct. We thank George Meigs and other Beamline staff at ALS, 8.3.1 for their help in  
862 data collection.

863

864 *QCRG Structural Biology Consortium.*

865 In addition to those listed explicitly in the author contributions, the structural biology portion of  
866 this work was performed by the QCRG (Quantitative Biosciences  
867 Institute Coronavirus Research Group) Structural Biology Consortium. Listed below are the  
868 contributing members of the consortium listed by teams in order of team relevance to the  
869 published work. Within each team the team leads are italicized (responsible for organization of  
870 each team, and for the experimental design utilized within each team), then the rest of team  
871 members are listed alphabetically. *CryoEM grid freezing/collection team: Caleigh M. Azumaya,*

872 *Cristina Puchades, Ming Sun, Julian R. Braxton, Axel F. Brilot, Meghna Gupta, Fei Li, Kyle E.*  
873 *Lopez, Arthur Melo, Gregory E. Merz, Frank Moss, Joana Paulino, Thomas H. Pospiech,*  
874 *Jr., Sergei Pourmal, Alexandra N. Rizo, Amber M. Smith, Paul V. Thomas, Feng Wang, Zanlin*  
875 *Yu. CryoEM data processing team: Miles Sasha Dickinson, Henry C. Nguyen, Daniel Asarnow,*  
876 *Julian R. Braxton, Melody G. Campbell, Cynthia M. Chio, Un Seng Chio, Devan Diwanji, Bryan*  
877 *Faust, Meghna Gupta, Nick Hoppe, Mingliang Jin, Fei Li, Junrui Li, Yanxin Liu, Gregory E.*  
878 *Merz, Joana Paulino, Thomas H. Pospiech, Jr., Sergei Pourmal, Smriti Sangwan, Raphael*  
879 *Trenker, Donovan Trinidad, Eric Tse, Kaihua Zhang, Fengbo Zhou. Crystallography team:*  
880 *Nadia Herrera, Huong T. Kratochvil, Ursula Schulze-Gahmen, Michael C. Thompson, Iris D.*  
881 *Young, Justin Biel, Ishan Deshpande, Xi Liu. Mammalian cell expression team: Christian Bache*  
882 *Billesbølle, Melody G. Campbell, Devan Diwanji, Carlos Nowotny, Amber M. Smith, Jianhua*  
883 *Zhao, Caleigh M. Azumaya, Alisa Bowen, Nick Hoppe, Yen-Li Li, Phuong Nguyen, Cristina*  
884 *Puchades, Mali Safari, Smriti Sangwan, Kaitlin Schaefer, Raphael Trenker, Tsz Kin Martin Tsui,*  
885 *Natalie Whitis. Protein purification team: Daniel Asarnow, Michelle Moritz, Tristan W. Owens,*  
886 *Sergei Pourmal, Caleigh M. Azumaya, Cynthia M. Chio, Amy Diallo, Bryan Faust, Meghna*  
887 *Gupta, Kate Kim, Joana Paulino, Jessica K. Peters, Kaitlin Schaefer, Tsz Kin Martin*  
888 *Tsui. Bacterial expression team: Amy Diallo, Meghna Gupta, Erron W. Titus, Jenny*  
889 *Chen, Roberto Efraín Díaz, Loan Doan, Sebastian Flores, Mingliang Jin, Huong T. Kratochvil,*  
890 *Victor L. Lam, Yang Li, Megan Lo, Gregory E. Merz, Joana Paulino, Aye C. Thwin, Stephanie*  
891 *Wankowicz, Zanlin Yu, Yang Zhang, Fengbo Zhou. Infrastructure team: David Bulkley, Arceli*  
892 *Joves, Almarie Joves, Liam McKay, Mariano Tabios, Eric Tse. Leadership team: Oren S*  
893 *Rosenberg, Kliment A Verba, David A Agard, Yifan Cheng, James S Fraser, Adam Frost,*  
894 *Natalia Jura, Tanja Kortemme, Nevan J Krogan, Aashish Manglik, Daniel R. Southworth, Robert*  
895 *M Stroud. The QCRG Structural Biology Consortium has received support from: Quantitative*  
896 *Biosciences Institute, Defense Advanced Research Projects Agency HR0011-19-2-0020 (to*  
897 *D.A.Agard and K.A.Verba; B. Shoichet PI), FastGrants COVID19 grant (K.A.Verba PI),*  
898 *Laboratory For Genomics Research (O.S.Rosenberg PI) and Laboratory for Genomics*  
899 *Research LGR-ERA (R.M.Stroud PI). R.M.Stroud is supported by NIH grants AI 50476,*  
900 *GM24485.*

901

## 902 **Author Contributions**

903 M.Schoof purified Spike\*, RBD, and ACE2 proteins, performed yeast display selections to  
904 identify and affinity mature nanobodies, expressed and purified nanobodies, tested activity in  
905 cell-based assays, cloned, expressed, and purified multivalent nanobody constructs, and

906 coordinated live virus experiments. B.Faust purified and characterized Spike\* protein and  
907 candidate nanobodies, developed, performed and analyzed SPR experiments for Spike\* and  
908 RBD-nanobody affinity determination, developed, performed and analyzed SPR binning,  
909 experiments, determined optimal freezing conditions for cryo-EM experiments, processed,  
910 refined and generated figures for Nb6, Nb11, and mNb6 EM datasets. R.Saunders expressed  
911 and purified ACE2 and nanobodies, developed and performed cell-based assays for inhibition of  
912 Spike\* binding and pseudovirus assays for determining nanobody efficacy. S.Sangwan  
913 expressed and purified Spike\*, RBD, ACE2-Fc, and nanobodies, processed cryo-EM data,  
914 optimized RBD-nanobody complexes for crystallography, grew crystals of mNb6, collected  
915 diffraction data, and refined the X-ray crystal structure of mNb6. V.Rezelj tested efficacy of  
916 nanobody constructs in live SARS-CoV-2 infection assays under the guidance of M.Vignuzzi.  
917 N.Hoppe purified nanobodies, developed, performed and analyzed SPR binning experiments,  
918 developed performed and analyzed variable Nb6-bi and Nb6-tri association experiments, and  
919 performed thermal melting stability assays for nanobody constructs. M.Boone developed  
920 approaches to express and purify nanobodies from *Pichia pastoris* and developed, performed,  
921 and analyzed approaches to quantify nanobody efficacy in live virus assays. C.Azumaya and  
922 C.Puchades determined optimal freezing conditions for cryo-EM experiments with B.Faust,  
923 optimized data collection approaches, and collected cryo-EM datasets. C.B.Billesbølle  
924 expressed and purified Spike\*, generated affinity maturation library for Nb6, and performed  
925 yeast display selections to identify mNb6. I.Deshpande expressed and purified nanobody  
926 constructs. J.Liang and C.B.Billesbølle built the yeast nanobody library enabling discovery of  
927 nanobodies in this study. B.Zha. performed live SARS-CoV-2 virus assays to test nanobody  
928 efficacy with guidance from O.Rosenberg. C.R.Simoneau and K.Leon performed live SARS-  
929 CoV-2 virus assays to test nanobody efficacy with guidance from M.Ott. K.M.White performed  
930 live SARS-CoV-2 virus assays to test nanobody efficacy with guidance from A.Garcia-Sastre.  
931 A.W.Barile-Hill performed SPR experiments with B.Faust. A.A.Anand, N.Dobzinski, B.Barsi-  
932 Rhyne, and Y.Liu. assisted in cloning, expression, and purification of nanobody and pseudovirus  
933 constructs. V.Belyy performed single-molecule nanobody-Spike\* interaction studies. S.Nock  
934 prepared media and coordinated lab usage during UCSF's partial shutdown. M.Zimanyi and  
935 S.Gupta performed radiolytic footprinting experiments with guidance from C.Ralston and  
936 analyzed mass spectrometry data generated by D.L.Swaney. Several members of the QCRG  
937 Structural Biology Consortium played an exceptionally important role for this project. A.Rizo,  
938 A.Smith, F.Moss collected cryo-EM data on Spike\*-nanobody complexes. S.Dickinson,  
939 H.Nguyen, K.Verba, C. Chio, U.S.Chio, M.Gupta, M.Jin, F.Li, Y.Liu, G.Merz, K.Zhang analyzed

940 cryo-EM data from 15 Spike\*-nanobody complex datasets. H.Kratochvil set up crystallization  
941 trials of various RBD-nanobody complexes, and crystallized, collected diffraction data for, and  
942 refined the mNb6 structure. M.Thompson collected, processed, and refined the mNb6 structure.  
943 D.Devanji and K.Schaefer expressed and purified Spike\*. A.Manglik expressed and purified  
944 Spike\*, labeled Spike\* for biochemical studies, designed selection strategies for nanobody  
945 discovery, cloned nanobodies for expression, designed affinity maturation libraries and  
946 performed selections, analyzed SPR data, and performed nanobody stability studies. The  
947 overall project was supervised by P.Walter and A.Manglik.

948

949 **Competing Interests**

950 M.Schoof, B.Faust, R.Saunders, N.Hoppe, P.Walter, and A.Manglik are inventors on a  
951 provisional patent describing anti-Spike nanobodies described in this manuscript.

952

953 **REFERENCES**

- 954 1. Ksiazek, T.G., et al., *A novel coronavirus associated with severe acute respiratory*  
955 *syndrome*. N Engl J Med, 2003. **348**(20): p. 1953-66.
- 956 2. Zaki, A.M., et al., *Isolation of a novel coronavirus from a man with pneumonia in Saudi*  
957 *Arabia*. N Engl J Med, 2012. **367**(19): p. 1814-20.
- 958 3. Zhou, P., et al., *A pneumonia outbreak associated with a new coronavirus of probable*  
959 *bat origin*. Nature, 2020. **579**(7798): p. 270-273.
- 960 4. Chan, J.F., et al., *A familial cluster of pneumonia associated with the 2019 novel*  
961 *coronavirus indicating person-to-person transmission: a study of a family cluster*. Lancet,  
962 2020. **395**(10223): p. 514-523.
- 963 5. Huang, C., et al., *Clinical features of patients infected with 2019 novel coronavirus in*  
964 *Wuhan, China*. Lancet, 2020. **395**(10223): p. 497-506.
- 965 6. Wu, F., et al., *A new coronavirus associated with human respiratory disease in China*.  
966 Nature, 2020. **579**(7798): p. 265-269.
- 967 7. Zhu, N., et al., *A Novel Coronavirus from Patients with Pneumonia in China, 2019*. N  
968 Engl J Med, 2020. **382**(8): p. 727-733.
- 969 8. World Health Organization. *WHO Coronavirus Disease (COVID-19) Dashboard*. 2020;  
970 Available from: <https://covid19.who.int/>.
- 971 9. Ke, Z., et al., *Structures, conformations and distributions of SARS-CoV-2 spike protein*  
972 *trimers on intact virions*. bioRxiv, 2020: p. 2020.06.27.174979.
- 973 10. Bosch, B.J., et al., *The coronavirus spike protein is a class I virus fusion protein:*  
974 *structural and functional characterization of the fusion core complex*. J. Virol., 2003.  
975 **77**(16): p. 8801-8811.
- 976 11. Cai, Y., et al., *Distinct conformational states of SARS-CoV-2 spike protein*. Science,  
977 2020.
- 978 12. Wang, Q., et al., *Structural and Functional Basis of SARS-CoV-2 Entry by Using Human*  
979 *ACE2*. Cell, 2020. **181**(4): p. 894-904.e9.
- 980 13. Yan, R., et al., *Structural basis for the recognition of SARS-CoV-2 by full-length human*  
981 *ACE2*. Science, 2020. **367**(6485): p. 1444-1448.
- 982 14. Walls, A.C., et al., *Structure, Function, and Antigenicity of the SARS-CoV-2 Spike*  
983 *Glycoprotein*. Cell, 2020. **181**(2): p. 281-292.e6.
- 984 15. Wrapp, D., et al., *Cryo-EM structure of the 2019-nCoV spike in the prefusion*  
985 *conformation*. Science, 2020. **367**(6483): p. 1260-1263.
- 986 16. Hoffmann, M., et al., *SARS-CoV-2 Cell Entry Depends on ACE2 and TMPRSS2 and Is*  
987 *Blocked by a Clinically Proven Protease Inhibitor*. Cell, 2020. **181**(2): p. 271-280.e8.
- 988 17. Shang, J., et al., *Structural basis of receptor recognition by SARS-CoV-2*. Nature, 2020.  
989 **581**(7807): p. 221-224.
- 990 18. Gupta, S., et al., *Synchrotron X-ray footprinting as a method to visualize water in*  
991 *proteins*. J Synchrotron Radiat, 2016. **23**(Pt 5): p. 1056-69.
- 992 19. Zhang, Y., et al., *Mapping the Binding Interface of VEGF and a Monoclonal Antibody*  
993 *Fab-1 Fragment with Fast Photochemical Oxidation of Proteins (FPOP) and Mass*  
994 *Spectrometry*. J Am Soc Mass Spectrom, 2017. **28**(5): p. 850-858.
- 995 20. Crawford, K.H.D., et al., *Protocol and Reagents for Pseudotyping Lentiviral Particles with*  
996 *SARS-CoV-2 Spike Protein for Neutralization Assays*. Viruses, 2020. **12**(5).
- 997 21. Kunz, P., et al., *The structural basis of nanobody unfolding reversibility and*  
998 *thermoresistance*. Sci Rep, 2018. **8**(1): p. 7934.
- 999 22. Baum, A., et al., *Antibody cocktail to SARS-CoV-2 spike protein prevents rapid*  
1000 *mutational escape seen with individual antibodies*. Science, 2020.
- 1001 23. Cao, Y., et al., *Potent Neutralizing Antibodies against SARS-CoV-2 Identified by High-*  
1002 *Throughput Single-Cell Sequencing of Convalescent Patients' B Cells*. Cell, 2020.  
1003 **182**(1): p. 73-84.e16.

- 1004 24. Chi, X., et al., *A neutralizing human antibody binds to the N-terminal domain of the Spike*  
1005 *protein of SARS-CoV-2*. Science, 2020.
- 1006 25. Ju, B., et al., *Human neutralizing antibodies elicited by SARS-CoV-2 infection*. Nature,  
1007 2020.
- 1008 26. Liu, L., et al., *Potent neutralizing antibodies directed to multiple epitopes on SARS-CoV-*  
1009 *2 spike*. Nature, 2020.
- 1010 27. Pinto, D., et al., *Cross-neutralization of SARS-CoV-2 by a human monoclonal SARS-*  
1011 *CoV antibody*. Nature, 2020. **583**(7815): p. 290-295.
- 1012 28. Rogers, T.F., et al., *Isolation of potent SARS-CoV-2 neutralizing antibodies and*  
1013 *protection from disease in a small animal model*. Science, 2020.
- 1014 29. Zost, S.J., et al., *Potently neutralizing and protective human antibodies against SARS-*  
1015 *CoV-2*. Nature, 2020.
- 1016 30. Leyva-Grado, V.H., et al., *Direct administration in the respiratory tract improves efficacy*  
1017 *of broadly neutralizing anti-influenza virus monoclonal antibodies*. Antimicrob Agents  
1018 Chemother, 2015. **59**(7): p. 4162-72.
- 1019 31. Detalle, L., et al., *Generation and Characterization of ALX-0171, a Potent Novel*  
1020 *Therapeutic Nanobody for the Treatment of Respiratory Syncytial Virus Infection*.  
1021 Antimicrob Agents Chemother, 2016. **60**(1): p. 6-13.
- 1022 32. Wrapp, D., et al., *Structural Basis for Potent Neutralization of Betacoronaviruses by*  
1023 *Single-Domain Camelid Antibodies*. Cell, 2020. **181**(5): p. 1004-1015.e15.
- 1024 33. Huo, J., et al., *Neutralizing nanobodies bind SARS-CoV-2 spike RBD and block*  
1025 *interaction with ACE2*. Nat. Struct. Mol. Biol., 2020.
- 1026 34. Walter, J.D., et al., *Sybodies targeting the SARS-CoV-2 receptor-binding domain*.  
1027 bioRxiv, 2020.
- 1028 35. Sun, Z., et al., *Potent neutralization of SARS-CoV-2 by human antibody heavy-chain*  
1029 *variable domains isolated from a large library with a new stable scaffold*. MAbs, 2020.  
1030 **12**(1): p. 1778435.
- 1031 36. Wu, Y., et al., *Identification of Human Single-Domain Antibodies against SARS-CoV-2*.  
1032 Cell Host Microbe, 2020. **27**(6): p. 891-898.e5.
- 1033 37. Esparza, T.J. and D.L. Brody, *High Affinity Nanobodies Block SARS-CoV-2 Spike*  
1034 *Receptor Binding Domain Interaction with Human Angiotensin Converting Enzyme*.  
1035 bioRxiv, 2020: p. 2020.07.24.219857.
- 1036 38. Hanke, L., et al., *An alpaca nanobody neutralizes SARS-CoV-2 by blocking receptor*  
1037 *interaction*. bioRxiv, 2020: p. 2020.06.02.130161.
- 1038 39. Custódio, T.F., et al., *Selection, biophysical and structural analysis of synthetic*  
1039 *nanobodies that effectively neutralize SARS-CoV-2*. bioRxiv, 2020: p.  
1040 2020.06.23.165415.
- 1041 40. Li, T., et al., *Potent synthetic nanobodies against SARS-CoV-2 and molecular basis for*  
1042 *neutralization*. bioRxiv, 2020: p. 2020.06.09.143438.
- 1043 41. Nieto, G.V., et al., *Fast isolation of sub-nanomolar affinity alpaca nanobody against the*  
1044 *Spike RBD of SARS-CoV-2 by combining bacterial display and a simple single-step*  
1045 *density gradient selection*. bioRxiv, 2020: p. 2020.06.09.137935.
- 1046 42. Chi, X., et al., *Humanized Single Domain Antibodies Neutralize SARS-CoV-2 by*  
1047 *Targeting Spike Receptor Binding Domain*. bioRxiv, 2020: p. 2020.04.14.042010.
- 1048 43. Stadlbauer, D., et al., *SARS-CoV-2 Seroconversion in Humans: A Detailed Protocol for a*  
1049 *Serological Assay, Antigen Production, and Test Setup*. Curr. Protoc. Microbiol., 2020.  
1050 **57**(1): p. e100.
- 1051 44. Lui, I., et al., *Trimeric SARS-CoV-2 Spike interacts with dimeric ACE2 with limited intra-*  
1052 *Spike avidity*. bioRxiv, 2020: p. 2020.05.21.109157.
- 1053 45. McMahon, C., et al., *Yeast surface display platform for rapid discovery of*  
1054 *conformationally selective nanobodies*. Nat. Struct. Mol. Biol., 2018. **25**(3): p. 289-296.



- 1055 46. Mastronarde, D.N., *Automated electron microscope tomography using robust prediction*  
1056 *of specimen movements*. J Struct Biol, 2005. **152**(1): p. 36-51.
- 1057 47. Zheng, S.Q., et al., *MotionCor2: anisotropic correction of beam-induced motion for*  
1058 *improved cryo-electron microscopy*. Nat Methods, 2017. **14**(4): p. 331-332.
- 1059 48. Punjani, A., et al., *cryoSPARC: algorithms for rapid unsupervised cryo-EM structure*  
1060 *determination*. Nat Methods, 2017. **14**(3): p. 290-296.
- 1061 49. Zivanov, J., et al., *New tools for automated high-resolution cryo-EM structure*  
1062 *determination in RELION-3*. Elife, 2018. **7**.
- 1063 50. Grant, T., A. Rohou, and N. Grigorieff, *cisTEM, user-friendly software for single-particle*  
1064 *image processing*. Elife, 2018. **7**.
- 1065 51. Lan, J., et al., *Structure of the SARS-CoV-2 spike receptor-binding domain bound to the*  
1066 *ACE2 receptor*. Nature, 2020. **581**(7807): p. 215-220.
- 1067 52. Rasmussen, S.G., et al., *Structure of a nanobody-stabilized active state of the  $\beta$ (2)*  
1068 *adrenoceptor*. Nature, 2011. **469**(7329): p. 175-80.
- 1069 53. Frenz, B., et al., *RosettaES: a sampling strategy enabling automated interpretation of*  
1070 *difficult cryo-EM maps*. Nat Methods, 2017. **14**(8): p. 797-800.
- 1071 54. Emsley, P. and K. Cowtan, *Coot: model-building tools for molecular graphics*. Acta  
1072 Crystallogr D Biol Crystallogr, 2004. **60**(Pt 12 Pt 1): p. 2126-32.
- 1073 55. Croll, T.I., *ISOLDE: a physically realistic environment for model building into low-*  
1074 *resolution electron-density maps*. Acta Crystallogr D Struct Biol, 2018. **74**(Pt 6): p. 519-  
1075 530.
- 1076 56. Adams, P.D., et al., *PHENIX: a comprehensive Python-based system for*  
1077 *macromolecular structure solution*. Acta Crystallogr D Biol Crystallogr, 2010. **66**(Pt 2): p.  
1078 213-21.
- 1079 57. Staus, D.P., et al., *Allosteric nanobodies reveal the dynamic range and diverse*  
1080 *mechanisms of G-protein-coupled receptor activation*. Nature, 2016. **535**(7612): p. 448-  
1081 52.
- 1082 58. Gupta, S., et al., *The Beamline X28C of the Center for Synchrotron Biosciences: a*  
1083 *national resource for biomolecular structure and dynamics experiments using*  
1084 *synchrotron footprinting*. J Synchrotron Radiat, 2007. **14**(Pt 3): p. 233-43.
- 1085 59. Yu, F., et al., *Fast quantitative analysis of timsTOF PASEF data with MSFragger and*  
1086 *IonQuant*. Mol Cell Proteomics, 2020.
- 1087 60. Choi, M., et al., *MSstats: an R package for statistical analysis of quantitative mass*  
1088 *spectrometry-based proteomic experiments*. Bioinformatics, 2014. **30**(17): p. 2524-6.
- 1089 61. Kabsch, W., *Automatic processing of rotation diffraction data from crystals of initially*  
1090 *unknown symmetry and cell constants*. Journal of Applied Crystallography, 1993. **26**(6):  
1091 p. 795-800.
- 1092 62. McCoy, A.J., et al., *Phaser crystallographic software*. J Appl Crystallogr, 2007. **40**(Pt 4):  
1093 p. 658-674.
- 1094 63. Bricogne G., B.E., Brandl M., Flensburg C., Keller P., Paciorek W., and S.A. Roversi P,  
1095 Smart O.S., Vornrhein C., Womack T.O. , *BUSTER version 1.10.0*. . Cambridge, United  
1096 Kingdom: Global Phasing Ltd., 2017.
- 1097